




TURBOMACHINERY & PUMP SYMPOSIA | HOUSTON, TX
SEPTEMBER 13-15, 2022
SHORT COURSES: SEPTEMBER 12, 2022

COMMISSIONING A NEW MULTIPHASE PUMP VISUALIZATION TEST RIG TO INVESTIGATE THE INTERNAL FLOW FIELD AND ITS CONNECTION WITH PUMP PERFORMANCE

Ted Ørjan Seim Gundersen 
PhD Candidate
University of Bergen
Bergen, Norway

Marine Dupouiron
Research Engineer
IFP Energies nouvelles
Solaize, France

Victor Moënne-Loccoz
Research Engineer
IFP Energies nouvelles
Solaize, France

Tim McAlinden
Research Technician
Schlumberger Cambridge Research
Cambridge, UK

Yngvar Cato Juliussen
Mechanical Engineer
OneSubsea, A Schlumberger Company
Bergen, Norway

Erik Andre Torbergsen
Processing Systems Engineering Manager
OneSubsea, A Schlumberger Company
Bergen, Norway

Andrew Meredith 
Programme Manager
Schlumberger Cambridge Research
Cambridge, UK

Svein-Arne Marthinussen
Technology Manager
OneSubsea, A Schlumberger Company
Bergen, Norway

Bjørn Johan Arntzen
Associate Professor
University of Bergen
Bergen, Norway

Alex Christian Hoffmann 
Professor
University of Bergen
Bergen, Norway

ABSTRACT

Pumps with helico-axial impellers are used to boost mixtures of gas and liquid, for instance in subsea production of unprocessed oil and gas. Experimental data is essential to fully understand and characterize the internal flow, as well as for validation and improvement of numerical modeling techniques. Here we describe the commissioning of a test rig that enables visualization and measurements of the pump's internal flow field. The test rig's pump unit design contains three impeller stages that are 50 percent downscaled relative to a full-scale version previously tested.

A reduction in nondimensional head, flow and efficiency relative to the full-scale pump can be attributed to lower Reynolds numbers and an increased relative impeller tip clearance. The tested head curves on single phase water exhibit a transition where the negative slope is replaced by a flat curve when reducing the volumetric flow rate below a certain value. Despite the downscaling, this change in slope occurs at the same relative flow rate as for the full-scale pump. This suggests that the test rig can be used to reproduce the characteristics of the full-scale performance and flow field in multistage pumps with helico-axial impellers. Varying the impeller tip clearance allowed for an estimate of pump head with the equivalent clearance as for the full-scale geometry. A Morrison number of 0.03 could then be established for the pump.

The impeller tip leakage flow and two recirculation zones in the diffuser channels were identified in a preliminary view of the internal flow field at two percent gas volume fraction and part-load operating conditions. Operation at low relative flow rates and high gas volume fractions led to system surge and slugging in the flow loop. Increasing the inlet pressure and temperature significantly improved the situation, allowing stable operation at lower relative flow rates. Modifications to avoid gas coalescence through the pump inlet could also further widen the operational envelope at high gas volume fractions.

INTRODUCTION

Pumps with helico-axial impellers are used to boost multiphase flows in several applications, for instance in subsea production of unprocessed oil and gas (Stenhaug, et al. 2019). During the last two decades, there has been a continuously increasing market demand of more powerful pump systems suitable for deep-sea field development, where a high differential pressure is required. With the increased power and pressure comes new challenges related to pump performance and rotordynamic stability (Bibet, et al. 2013). For these applications, the pumps may generate a differential pressure up to 200 bar and have a power rating up to 4 MW.

Normally, helico-axial pumps have a multistage design consisting of several helico-axial impellers and diffusers, so-called compression cells. The compression cells developed in the POSEIDON project, a collaboration project launched in 1984 between IFP Energies nouvelles (IFPEN) and industry partners, are designed to handle all gas volume fractions (GVF) and have a wide operating range in terms of relative flow rate. More information on the development and early experience with helico-axial pumps can be found in Falcimaigne and Decarre (2008) and Cooper, et al. (1996). See also the relevant patent documentation by Arnaudeau (1993). The axial flow design contributes to the excellent gas-handling capabilities, as the centrifugal and Coriolis forces acting on the fluid in the impeller have opposite signs, which impairs phase separation. Furthermore, the impeller and diffuser have characteristic geometrical features that will significantly affect the internal flow field and its dynamics during operation. For example, the impeller is open and there is a free passage for the process fluid through a tight gap between the blade and the pump housing. Flow through this gap contributes to redistribution of fluid between the impeller channels and can promote mixing of the phases in multiphase conditions. The significance of secondary flows and other features of the flow field will depend on pump operating conditions. This can in turn explain the performance and stability characteristics of the pump.

Given the complex internal flow field, experimental results are essential to fully understand and characterize the flow. Efforts to further enhance pump performance or achieve a wider operation envelope by improving dynamic stability within the compression cell, would clearly benefit from this knowledge. We cannot rely on numerical simulations alone to replicate the complex structures and dynamics of the flow. Experimental data is therefore crucial for validation and improvement of numerical modeling techniques, especially when considering part-load pump operation or multiphase flow. An experimental setup that enables visualization and measurement of the internal flow in such a compression cell will provide valuable insight for pump designers.

Experimental setups built for the purpose of flow visualization and measurements in helico-axial compression stages include a three-stage horizontal setup described in El Hajem, et al. (2001) and Vilagines, et al. (2003). A high-speed camera and laser Doppler velocimetry measurements were used to investigate the internal flow field at varying flow rates for single phase operation and with bubbly flow. The amount of published data from this test campaign is however scarce. More recently, several experiments involving flow visualization and performance assessment of helico-axial compression cells in horizontal three-stage setups have been described by Zhang, et al. (2015), Zhang, et al. (2016) and Xu, et al. (2019). Tests were conducted with up to approximately 50 percent gas volume fraction, with images of internal flow regimes observed when varying the gas flow rate. Gudigopuram (2016) describes a single-stage setup for a helico-axial compression cell where a high-speed camera was used to visualize the internal flow field at up to 8 percent gas volume fraction. The impeller and diffuser were manufactured in a clear stereolithography material where the thickness of the impeller blades had to be increased by 50 percent to improve robustness.

Several studies have investigated the characteristics of multiphase flow in axial flow inducers and mixed flow compression cells, which can resemble the helico-axial design. Recent work related to cavitating inducers and multiphase flow in inducers includes an axial-flow test rig described by Rapposelli, et al. (2002) and a test rig for centrifugal impellers with an upstream inducer Mansour, et al. (2019). Barrios (2007) and Gamboa and Prado (2010) describe a visualization test rig for a single-stage mixed flow geometry based on a design for downhole electrical submersible pumps (ESP). Dupoirion (2018) commissioned and conducted experiments with a visualization test rig for a multistage setup of mixed flow cells for ESPs. Serena and Bakken (2015) built a single-stage setup with an unshrouded mixed flow compression cell and Miyabe, et al. (2005) describe flow instabilities in a low-specific speed mixed flow pump.

Due to the potentially high pressures involved with multistage pumping, the compression cells in visualization test rigs are normally of a moderate diameter to stay within the design pressure of the transparent material, often acrylic glass. Previous studies on helico-axial compression cells are often compared with numerical analysis results but are lacking a performance comparison with an upscaled geometry, which is relevant in commercial applications. The present work describes the commissioning of a visualization test rig where the hydraulic performance of a downscaled compression cell can be compared with its full-scale counterpart. It is a part of an initiative to further improve and validate numerical modeling techniques for simulation of hydraulic performance, unsteady fluid-structure interaction forces and the related rotordynamic stability of helico-axial multiphase pumps.

HELICO-AXIAL VISUALIZATION RIG

An illustration of the rig is shown in Figure 1. The conceptual work on the Helico-Axial Visualization Rig (HAVR) initiated in 2015. HAVR was designed in a collaboration project between OneSubsea and Schlumberger Cambridge Research (SCR) where the purpose was to make a setup for research on axial pump performance and internal flow regimes. HAVR was assembled at SCR and initial tests were conducted in 2017 and 2018. After a period of inactivity, the rig was commissioned at IFPEN's facilities in Solaize, outside Lyon, France in 2021. Several upgrades have been installed and an initial test campaign with a selected hydraulic design has been performed during 2021 and 2022.

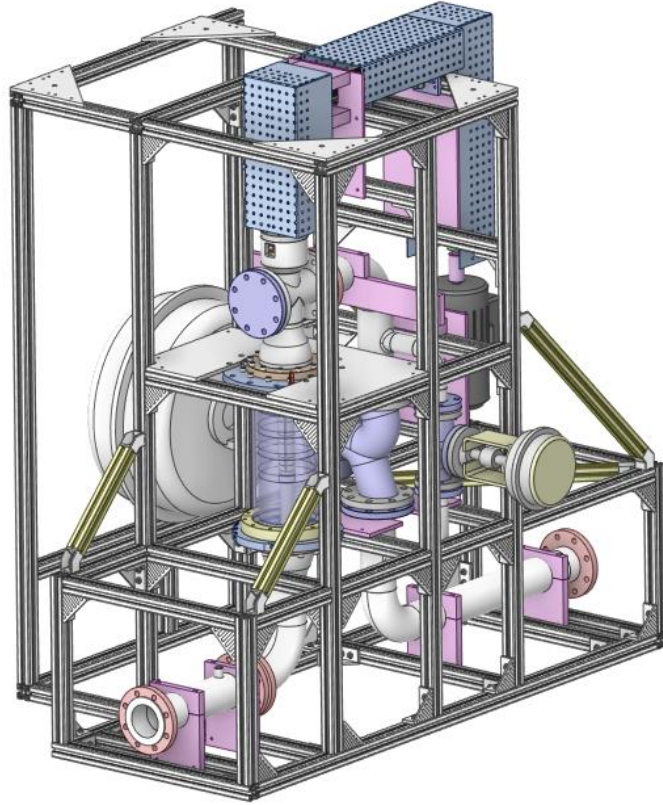


Figure 1. Illustration of HAVR

Test Rig Design

An overview of the test rig components can be seen in Figure 2. HAVR is designed as a skid which can be moved in and out of an experimental flow loop as a unit. The frame is made from aluminum profiles and can easily be modified, if needed. The process fluid pipe spools are 4 inch stainless steel, connecting the pump unit with two pneumatically actuated globe valves. The valves are installed in a parallel configuration downstream of the pump and are used to provide back pressure and control the flow rate through the pump. Coarse regulation is done with a 4 inch valve, while finer control is obtained by using the 2 inch valve in parallel. An electric motor is connected to the pump shaft train through a belt. The motor is equipped with an encoder that can be used to record the angular position of the shaft. A torque meter is installed on the pump shaft train to measure torque and rotation speed. Lubrication of the mechanical seal on the pump shaft is provided by an external system which pumps water through the seal with overpressure relative to the pump discharge pressure. For safety, a pressure relief valve can be installed on the discharge side through a flanged connection.

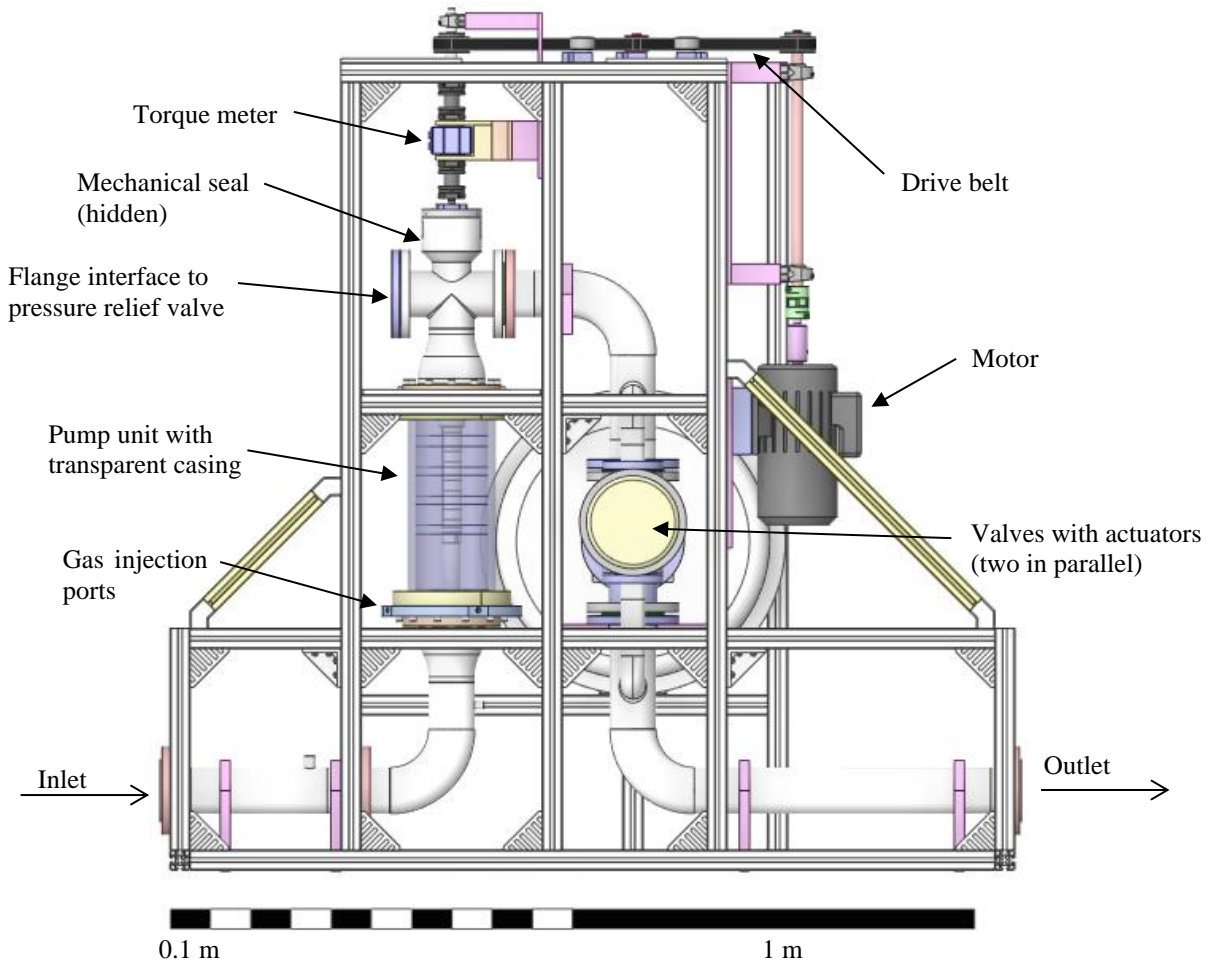


Figure 2. Components of HAVR

A set of three commercial mass flow controllers are installed on the rig and can be connected to a source of pressurized gas. They provide a controlled flow rate of Nitrogen through flexible tubing connected to pump unit inlet flange. Air could alternatively be used as the gas phase. Nitrogen was however readily available at the facility and is used throughout the present test campaign. The main design specifications for the rig are given in Table 1.

Table 1. HAVR specifications

Pump type	Rotodynamic, multistage, multiphase pump
Piping specification	4 inch schedule 10, AISI316L
Design pressure	16 bara
Process fluids	Water, Nitrogen
Motor rated power	15 kW
Motor rated torque	47.7 Nm
Maximum design speed	3000 rpm
Gas controller capacity (Nitrogen)	0.04 - 350 m ³ /h at standard conditions
Nominal impeller outer diameter	165 mm

Pump Unit

Subsea multiphase pumps are installed and operated vertically to reduce their footprint and to facilitate the mixing of the incoming fluids from the well. Steady and homogeneous impeller inlet flow conditions are beneficial in terms of obtaining stable system operation and optimal pump performance. A typical helico-axial pump configuration for subsea boosting can be seen in Bibet, et al. (2013). In order to reduce erosion rates due to solid particles in the flow, as well as to limit the Mach number and centrifugal forces, the design speed is normally limited to 4600 rpm. This contributes to a low design specific speed N_D , and several compression cells in series are required to achieve the desired head. Thus, the performance and flow dynamics in a series of compression cells is the most relevant setup to study. HAVR is therefore adapted for three compression cells in series and a vertical configuration is maintained to avoid unfavorable impact of the gravitational force, especially in the inlet section.

A transparent pump casing is manufactured from acrylic glass (PMMA). The wall thickness is 20 mm. Although the design pressure is 16 bara, the acrylic glass is sensitive to scratches and cracks which would reduce its strength. As a conservative safety measure, the maximum operating pressure is therefore limited to 6 barg while using the transparent casing. An illustration of the pump unit can be seen in Figure 3.

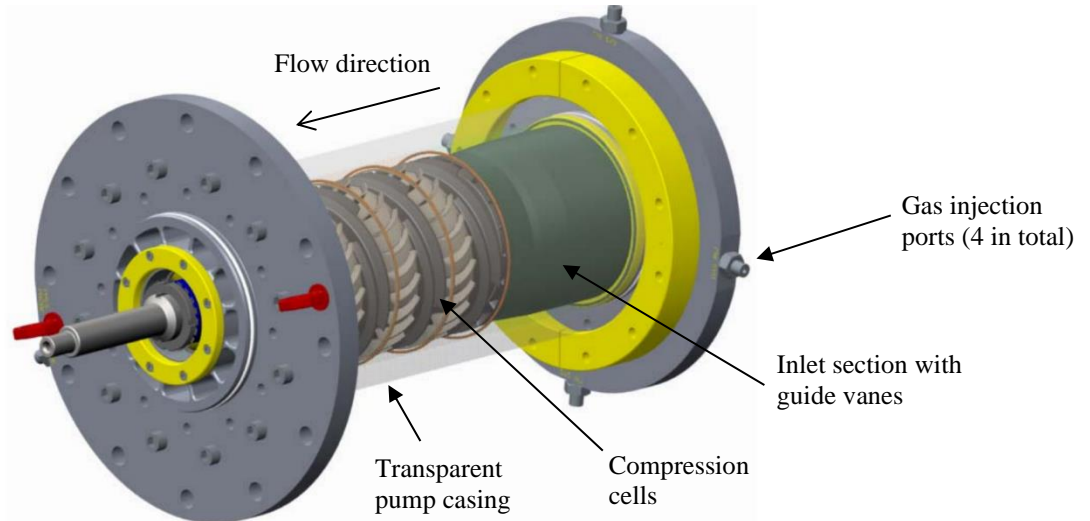


Figure 3. Illustration of HAVR Pump Unit with Transparent Casing

The pump casing holds the pump unit assembly together through the inlet and outlet stainless steel flanges. A ball bearing which supports the pump shaft is installed in each flange. A pump inlet section was 3D-printed in a polymer material and is installed upstream of the impellers. The gas and liquid phases are mixed in this section before the multiphase flow passes through a set of inlet guide vanes directly upstream the first impeller. The main purpose of the inlet guide vanes is to limit pre-rotation of the fluid at the impeller inlet. A set of three identical compression cells are installed in HAVR for the current test campaign. They are 50 percent downscaled relative to a compression cell previously tested in a three-stage configuration. The nondimensional specific speed N_D at the best efficiency point is relatively low, approximately 0.72 ($N \sim 1970$ in US Customary Units; rpm, gpm, ft) for a single full-scale compression cell in single phase conditions, where

$$N_D = \frac{\Omega Q^{\frac{1}{2}}}{(gH)^{\frac{3}{4}}}. \quad (1)$$

Ω is the shaft rotation in rad/s, g is the gravitational constant, Q is the volumetric flow rate, and H is the head generated by the compression cell.

Impeller

The impellers are machined stainless steel components with the same maximum surface roughness specification as for the full-scale impellers, $Ra = 1.6 \mu m$. It is desirable with a dark and matt surface in order to reduce reflections during flow visualization and laser doppler velocimetry (LDV) experiments. The impellers have therefore been surface treated with a black-oxide finish. The black oxidation process does not alter the dimensions of the impellers and geometric similarity with the full-scale design is maintained. Note that also 3D-printed impellers could be installed in HAVR, but care must be taken with regards to the surface roughness of the blades and the hub; Sanding or other types of surface treatment may be needed to reduce the relative roughness which impacts pump performance. Such surface treatment can contribute to deteriorated geometric similarity, especially in terms of a uniform impeller tip diameter and a sharp edge between the tip and pressure/suction sides of the blade.

The main geometric properties of the impeller design are given in Table 2. Note that the given blade thickness at tip decreases slightly towards the leading and trailing edges. The blades have a cambered profile, i.e. $\beta_{b2T} > \beta_{b1T}$.

Table 2. Impeller Geometric Properties

Nominal tip radius R_T	82.5 mm
Number of blades	4
Nominal inlet blade height b_1	12.25 mm
Blade tip inlet angle β_{b1T}	3.7 degrees
Blade thickness at tip	2.5 mm
Axial length (hub)	34 mm

The manufactured impellers are depicted in Figure 4.

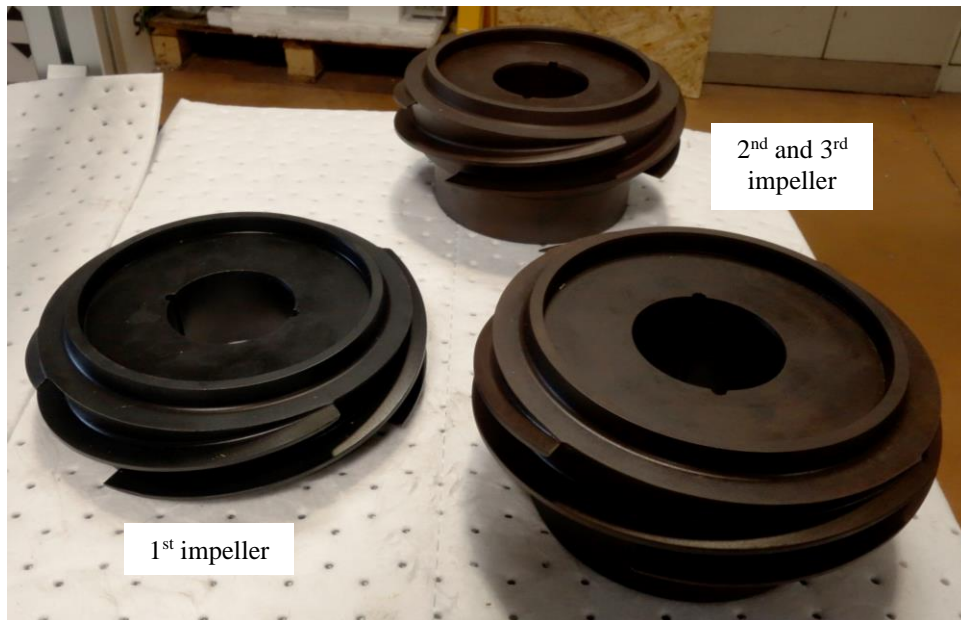


Figure 4. HAVR Helico-Axial Impellers. The Hydraulic Design is Identical in all Three Stages. The Second and Third Stage Impellers (Right-Hand Side) Have an Upstream Extension which is Located Behind the Hub of the Upstream Diffuser when Assembled. See Also Figure 7.

Diffuser

Diffusers for helico-axial impellers are normally designed with a relatively short axial length to keep the overall shaft length short in a multistage setup. Their main purpose is to straighten the flow and provide favorable inlet conditions for the next impeller. A short axial length can help to reduce separation and velocity slip between the phases through the diffuser. In HAVR, the diffuser vanes and their hub structure are 3D-printed in a black polymer material and assembled in an acrylic glass cylinder. The acrylic glass is polished for visualization purposes and the diffuser vanes are manually sanded to reduce the surface roughness. A typical roughness $Ra \approx 9 \mu m$ was measured on the hub and pressure side of a blade after sanding, but this must be regarded as an indication only, due to the manual sanding process. When assembled in the pump unit, the diffuser assembly with the cylinder extends upstream along the impeller and forms the shroud surface for the whole compression cell.

Figure 5 depicts a 3D-printed diffuser after sanding. An illustration of the diffuser assembly can be seen in Figure 6. There are 23 vanes and the axial length of the hub is 35.5 mm. The thickness of the vanes is 2 mm. The three diffusers installed in HAVR for the present test campaign were identical.



Figure 5. HAVR Helico-Axial 3D-Printed Diffuser Hub Structure with Vanes. The Diffuser was Manually Sanded to Reduce the Surface Roughness.

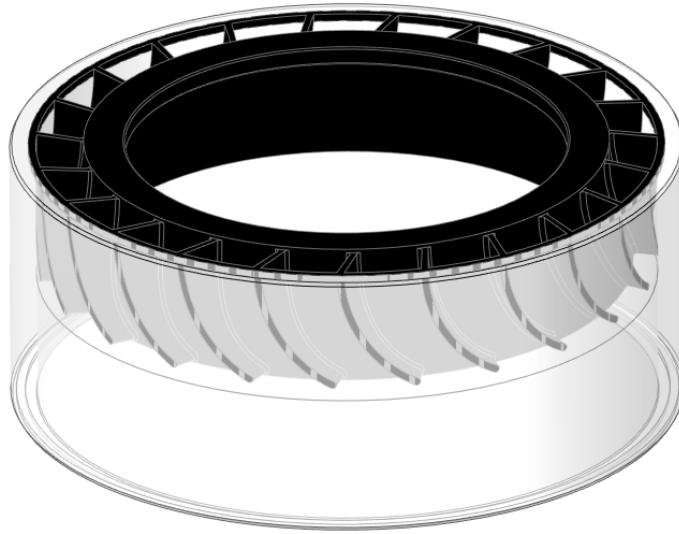


Figure 6. Illustration of HAVR Diffuser Assembly

Tip Gap Analysis

The geometry of the gap (both radial clearance and blade thickness at tip) between an unshrouded impeller and the stationary pump casing can significantly impact both pump performance and the internal flow field characteristics. Secondary flows will occur due to the leakage of fluid from the pressure side to the suction side of the impeller blades. An increased gap will lead to an increased leakage rate, which generally reduces pump efficiency and its capability to generate head (Gulich 2020).

Obtaining geometric similarity of the tip gap clearance on the current downscaled helico-axial compression cell is challenging due to the looser tolerances involved when machining and polishing acrylic glass, relative to steel components. But perhaps more importantly is the impact of temperature; With regards to thermal expansion, acrylic glass is more sensitive to temperature variations, relative to steel. During operation of HAVR, the temperature of both impellers and diffuser assemblies will converge towards the process fluid temperature. Due to the difference in coefficients of thermal expansion, the diffuser assembly may expand or contract more than the impeller and thus the clearance between them will vary. This will in turn have an impact on pump performance and secondary flows.

Figure 7 illustrates the assembled geometry near the second compression cell. During pump assembly, the diffuser cylinders are stacked on top of each other with a small clearance to the internal diameter of the pump casing. O-rings between the cylinders ensure a single closed volume between the diffuser assemblies and the pump casing in its full axial length. The pressure in this volume, or rather the pressure difference across the diffuser cylinder wall, will also impact the diameter of the cylinder and thus the tip clearance.

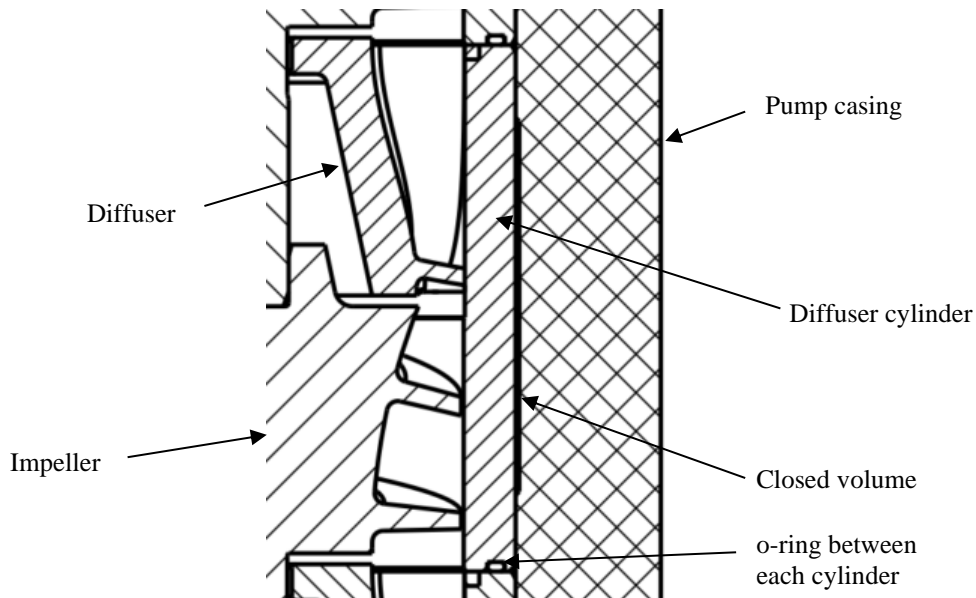


Figure 7. Cross-Sectional View of HAVR Second Stage Compression Cell

To have better knowledge of the actual tip gap during pump operation, an axis-symmetric finite element model (FEM) was established in a commercial software, which considers both temperature and pressure differences in the assembly. For this model to provide meaningful results, accurate input values are essential; The impeller outer diameter and diffuser cylinder inner diameter were measured with micrometers at a given steady state temperature prior to assembly. Secondly, the closed volume between the cylinders and the pump casing is liquid filled and the pressure is monitored and can be controlled by the operators during testing. By running the pump for a sufficient amount of time before recording experiments, the temperature of the impellers and diffusers can be assumed equal to the measured process fluid temperature. After the test campaign, the measured temperature can be used together with the recorded pressure at the inlet, outlet and in the closed volume to estimate an actual tip clearance during operation. An example of such a result from the finite element model is shown in Figure 8.

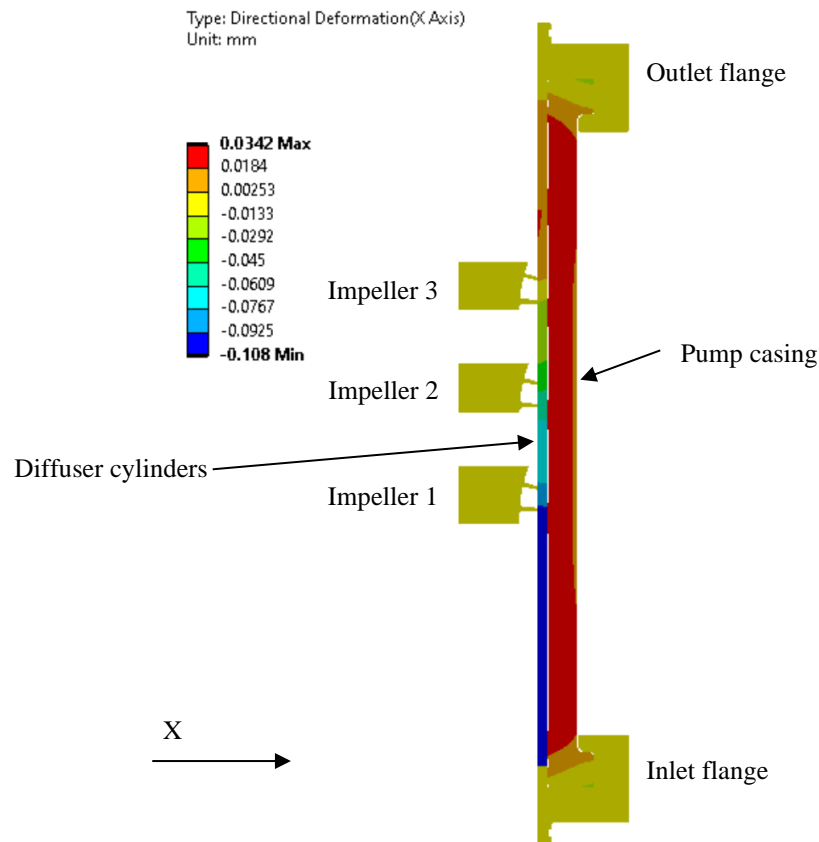


Figure 8. Example of FEM Estimated Horizontal Deformation in HAVR During Operation, Relative to During Assembly. Pump Casing is Expanded Horizontally, while the Diffuser Cylinders Contract or Expand Depending on the Local Conditions.

For the assembly presented in the current report, the average radial tip gap (clearance), denoted s , was 0.48 mm during assembly at a room temperature of 19° C. This is more than the nominal downscaled value and the deviation is mainly due to a “too large” shroud diameter; The as-built diameter of the impellers is 99.9 percent of the downscaled values. Although geometric similarity may not be achieved for the radial clearance in the impeller tip gap, relative to a full-scale design, the important factor is to have knowledge of the actual tip gap so that this can be taken into account when interpreting test results. Further, for the purpose of validation and improvement of numerical modeling techniques applied to full-scale designs, the relevant prerequisite is being able to simulate the actual tested geometry. Given, of course, that the relative tip gap s/b_1 is within a reasonable range so that the qualitative characteristics of the flow remain the same.

Visualization Box

The view of the pump unit internals is initially distorted due to the refraction angle through the pump casing. By immersing the casing in water, inside a square visualization box made from acrylic glass, refraction angles are minimized by the now flat air/water interface across the box wall. The view of the pump internals is thereby improved. An illustration of the visualization box is seen in Figure 9. The box is clamped onto the pump with seals at the interfaces.

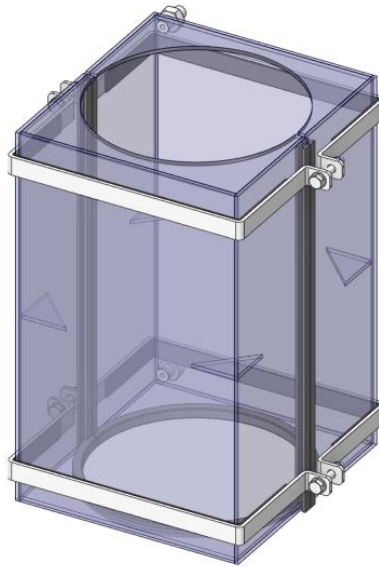


Figure 9. Illustration of Visualization Box that can be Mounted on the Transparent Pump Casing to Improve the View of Pump Internals

Figure 10 depicts a portion of the pump unit with the visualization box installed. Filling of the visualization box with water is ongoing and the improved view of the pump internals is visible across the liquid level.

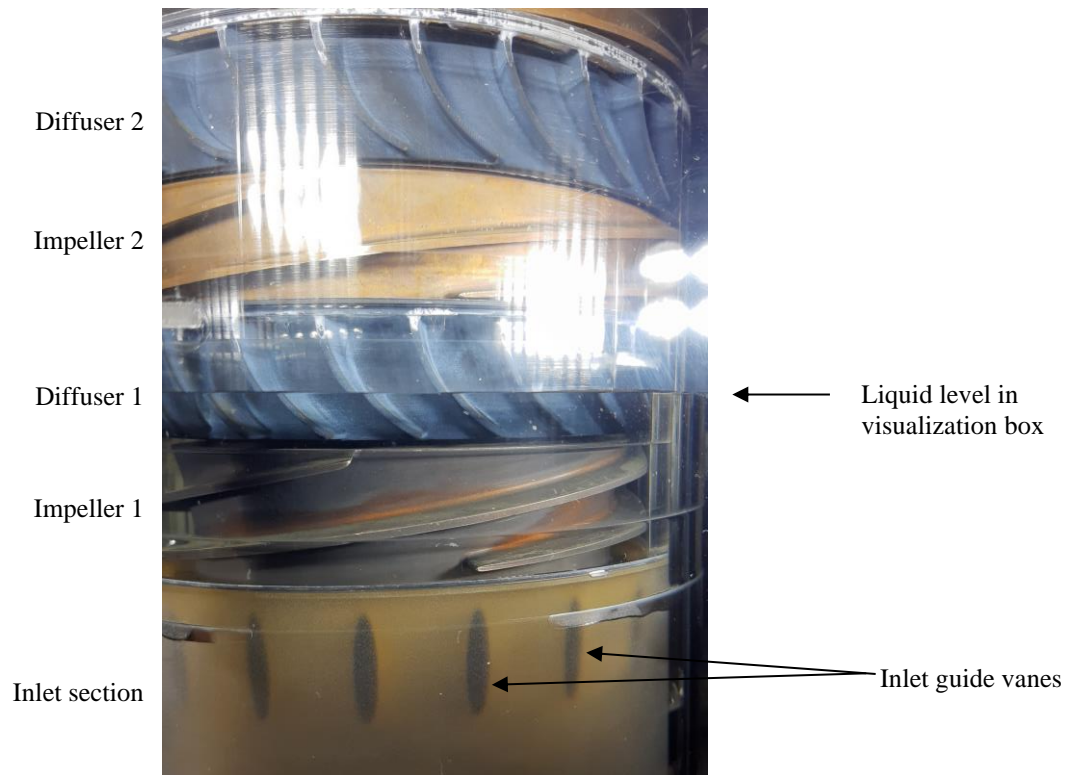


Figure 10. Picture of Water-Filled Pump Unit with Visualization Box Installed. Filling of Visualization Box with Water is Ongoing and the Effect on the View of the Compression Cells can be Seen Across the Liquid Level.

Flow Loop

HAVR was installed in a multiphase flow loop. A simplified process flow diagram is shown in Figure 11. The design pressure of the loop is 10 bara. For the current experiments, the separator ventilated to ambient pressure. Two pumps upstream HAVR were used to control the inlet pressure and to compensate the pressure drop in the loop so that HAVR could be tested also at the highest relative flow rates. The liquid flow rate and density ρ were measured by a Coriolis flow meter upstream HAVR. Pump inlet and outlet pressures are measured in the respective pump unit flanges, p_1 and p_2 , respectively. The liquid temperature is measured in the inlet piping (not shown).

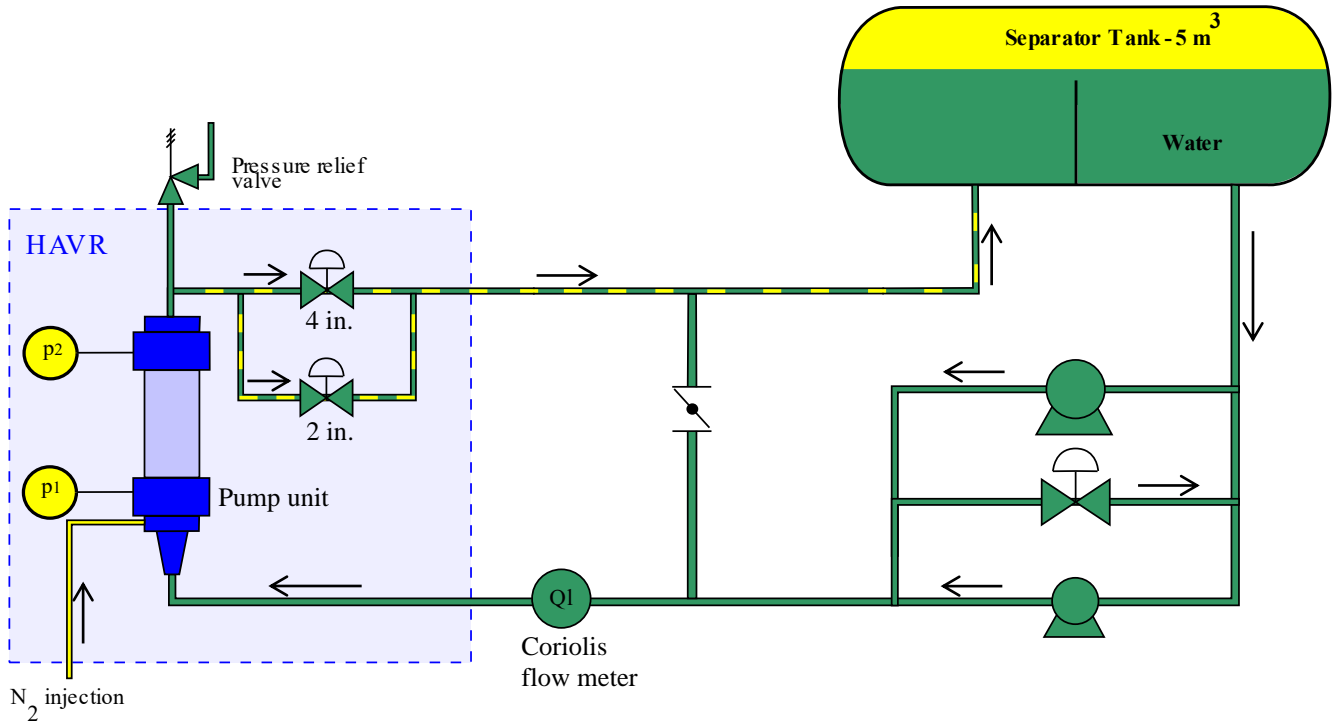


Figure 11. Simplified Process Flow Diagram of HAVR in the Experimental Flow Loop. Flow Direction Indicated by Arrows.

Interfaces

A schematic overview of the interfaces between HAVR and other parts of the system is shown in Figure 12. Control of HAVR and data acquisition from its instrumentation was handled by a customized setup in a commercial software, running on a computer connected to HAVR's electrical cabinet. A variable-frequency drive (VFD) controlled the HAVR motor speed and was operated through a separate flow loop control system. Nitrogen (injected gas) and air (for valve actuators) were supplied from a centralized system at the facility.

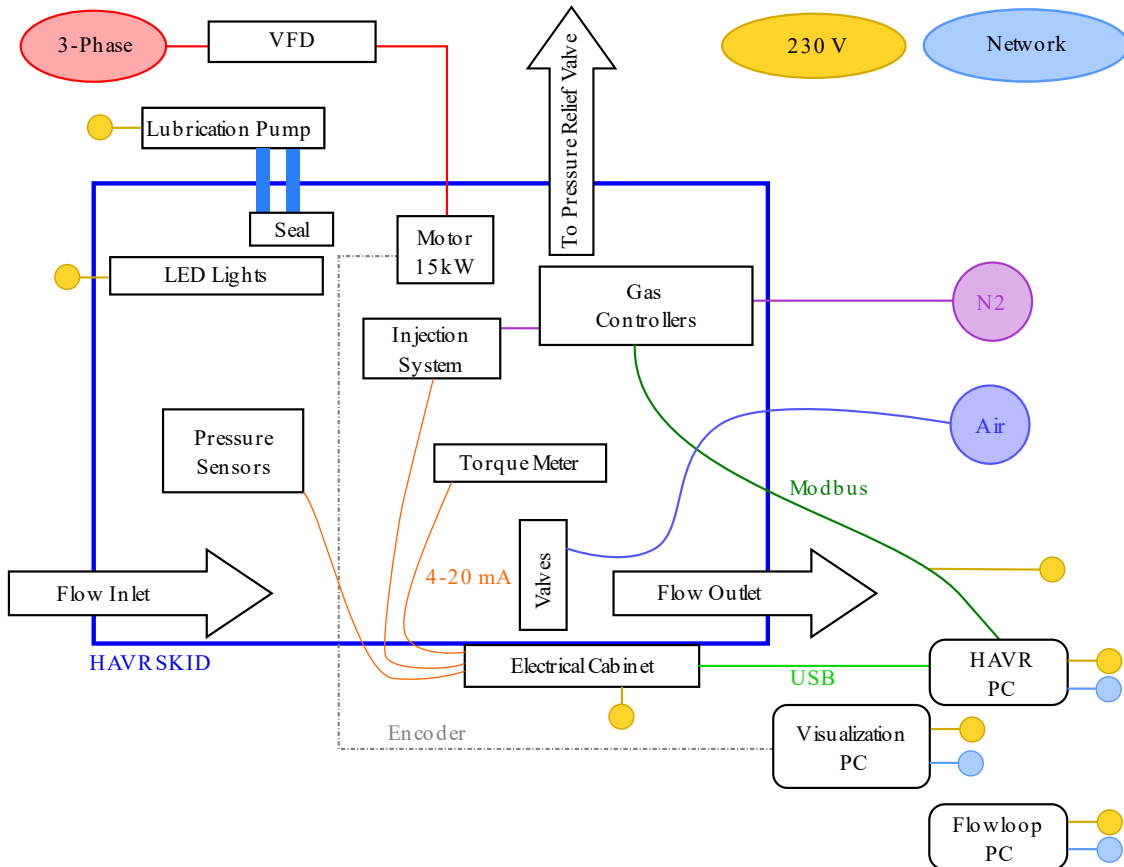


Figure 12. HAVR System Interfaces

Commissioning Campaign

The test campaign was initiated with an assessment of the mechanical losses in HAVR, before the performance in single phase and multiphase conditions was evaluated.

Mechanical Loss

Losses (i.e. torque) related to the shaft bearings and mechanical seal was assessed to be able to estimate the efficiency of the compression cells. Steel rings without blades replaced the impellers on the shaft and the pump was run at varying speed, filled with water. The results could be approximated by a linear model for the measured torque as function of pump speed up to 2500 rpm. At 2000 rpm, the model yields 2.8 Nm. However, as the test campaign spanned a full year, wear and potential corrosion in the bearings can impact the mechanical losses over time. This model is therefore rather uncertain. In future test campaigns, mechanical losses could rather be assessed by running HAVR with the impellers installed, in nitrogen at low pressure, directly prior to or after each performance test.

Single Phase Operation

A basis for a multiphase pump performance model can be established under single-phase operating conditions with an incompressible fluid. For multiphase operation, degradation factors depending on e.g. GVF and phase density ratio can be applied to the single-phase performance, as described by Falcimaigne and Decarre (2008) and Gülich (2020).

The static differential pressure, $dp = p_2 - p_1 + \rho gh$, generated by the pump with single phase water as process fluid is shown for different speed curves in Figure 13. h is the vertical length between the pump outlet and inlet and g is the gravitational constant. The curves exhibit a consistent behavior for the speed range of 1000 to approximately 2000 rpm.

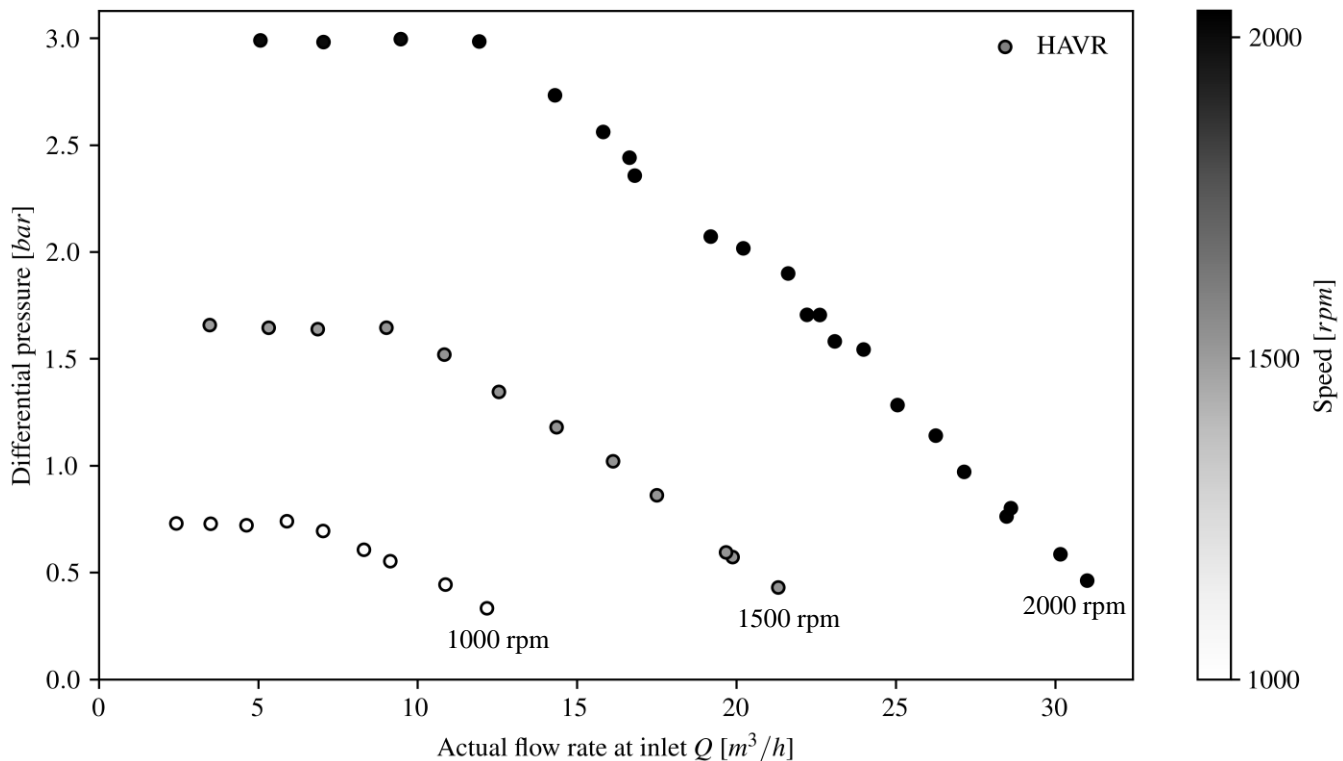


Figure 13. HAVR Differential Pressure – Single Phase Water. Pump Speed in Greyscale. Test Curves Identified by Notes of Approximate Speed.

The points around 2000 rpm are recorded at different occasions and there is seemingly a small variation in the generated differential pressure. To account for differences in speed and fluid density, the curves can be plotted nondimensionally. The flow coefficient is defined as

$$\phi_1 = \frac{Q}{A_1 R_T \Omega} \quad (2)$$

and the head coefficient as

$$\psi = \frac{dp}{\rho (R_T \Omega)^2}. \quad (3)$$

The total volumetric flow rate (liquid and gas phase) is denoted Q , A_1 is the impeller inlet area (hub to shroud at leading edge), R_T is the impeller tip radius and Ω is the radian frequency of the shaft rotation. The data points from Figure 13 are plotted in terms of ϕ_1 and ψ in Figure 14.

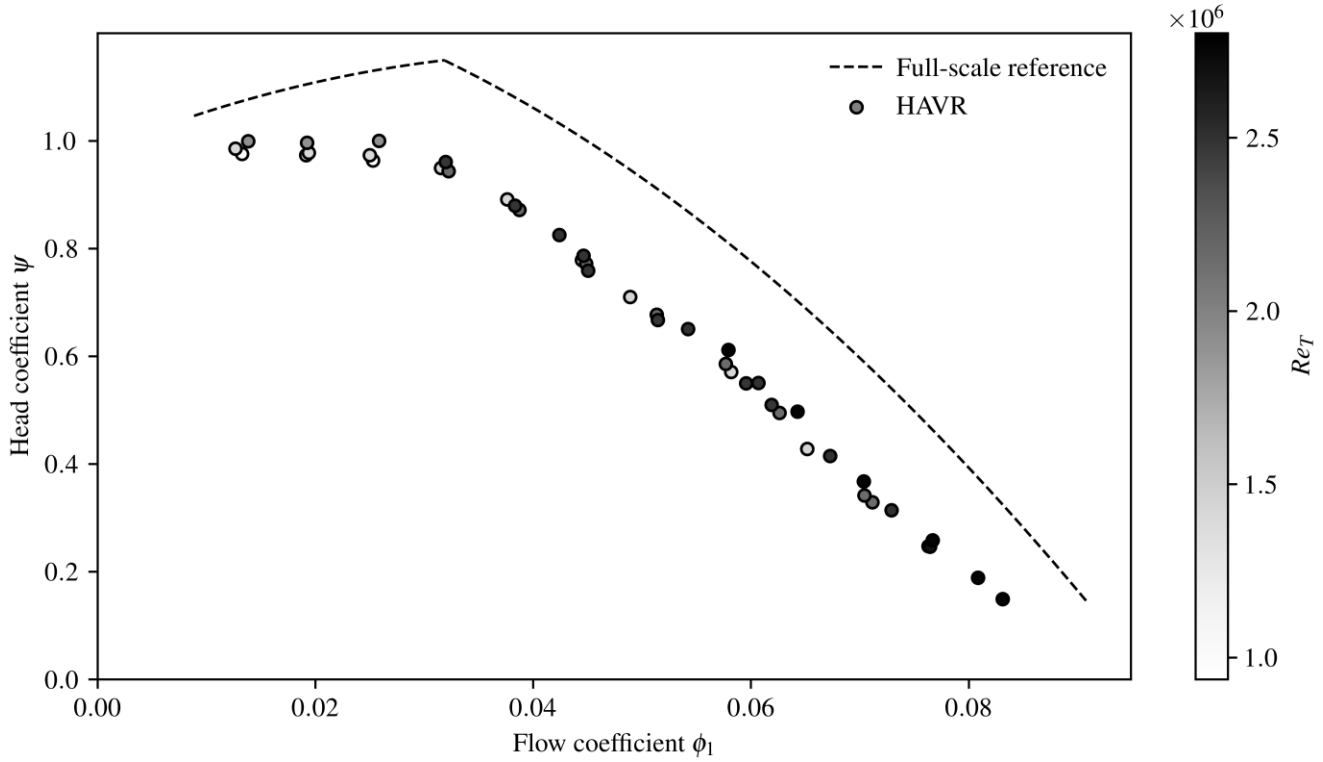


Figure 14. Nondimensional Differential Pressure Comparison – Single Phase Water. Tip-Speed Reynolds Number for Each Test Point in Greyscale.

The tested data points align quite well. The curve has an obvious shift from a negative slope to a relatively flat profile below a certain flow coefficient. This would be a natural point to define as the minimum flow rate for the compression cell, in order to avoid the excessive dynamic loads (e.g. due to rotating stall) which are normally associated with operation at flow rates below this value. Reference data from a full-scale test of the same compression cell in a three-stage setup is represented by a dashed line in the figure. The line is a best-fit polynomial based on a total of 86 test points performed during single phase operation. The head-flow curves resemble each other, but the full-scale curve exhibit both higher head and flow capacity. Two main factors can contribute to the deviation, namely “Reynolds number effects” and the lack of geometric similarity due to a discrepancy in the relative impeller tip gap size. These will be discussed subsequently.

Some of the losses in the pump are Reynolds-number dependent. Generally, a reduction of the Reynolds number causes a degradation in performance, highly relevant when pumping viscous fluids for instance. Like friction losses in turbulent pipe flow, the performance degradation becomes more sensitive to Reynolds number variations as the Reynolds number decreases. At sufficiently high Reynolds numbers, the relevant losses become more and more independent of Reynolds number and the pump performance will converge. To investigate this effect, the tip-speed Reynolds number

$$Re_T = \frac{2\rho\Omega R_T^2}{\mu} \quad (4)$$

is calculated for each test point and shown by a greyscale in Figure 14. μ is the dynamic viscosity of the fluid. The main driver for variations in Re_T is pump speed, but variations in viscosity at different temperatures can also be significant. From the figure it is seen that HAVR was operated at Reynolds numbers around 2×10^6 , whereas for the full-scale test, Re_T was approximately 3×10^7 due to the larger impeller diameter. This one-order-of-magnitude difference can contribute significantly to the observed performance deviation.

For the HAVR results alone, a minor shift in the head curve with Re_T seems apparent at medium and high flow coefficients, but the data set is not conclusive, there are still variations between test points with the same Reynolds number. This leads us to the discussion of the relative tip gap size s/b_1 .

Figure 15 shows the efficiency η relative to the maximum efficiency of the full-scale geometry η_{max} . For single phase operation, the efficiency is

$$\eta = \frac{Qdp}{\Omega T}, \quad (5)$$

where T is the torque. Only HAVR data points from the 2000 rpm curve are included, as these are the points where the impact of uncertainty in HAVR mechanical losses is smallest. First, the characteristic of the efficiency as a function of flow coefficient resembles the full-scale reference well, but there is a reduction in efficiency which increases with flow coefficient. The best efficiency point (BEP) is shifted to a lower flow coefficient and the drop at high flow rate appears earlier for HAVR.

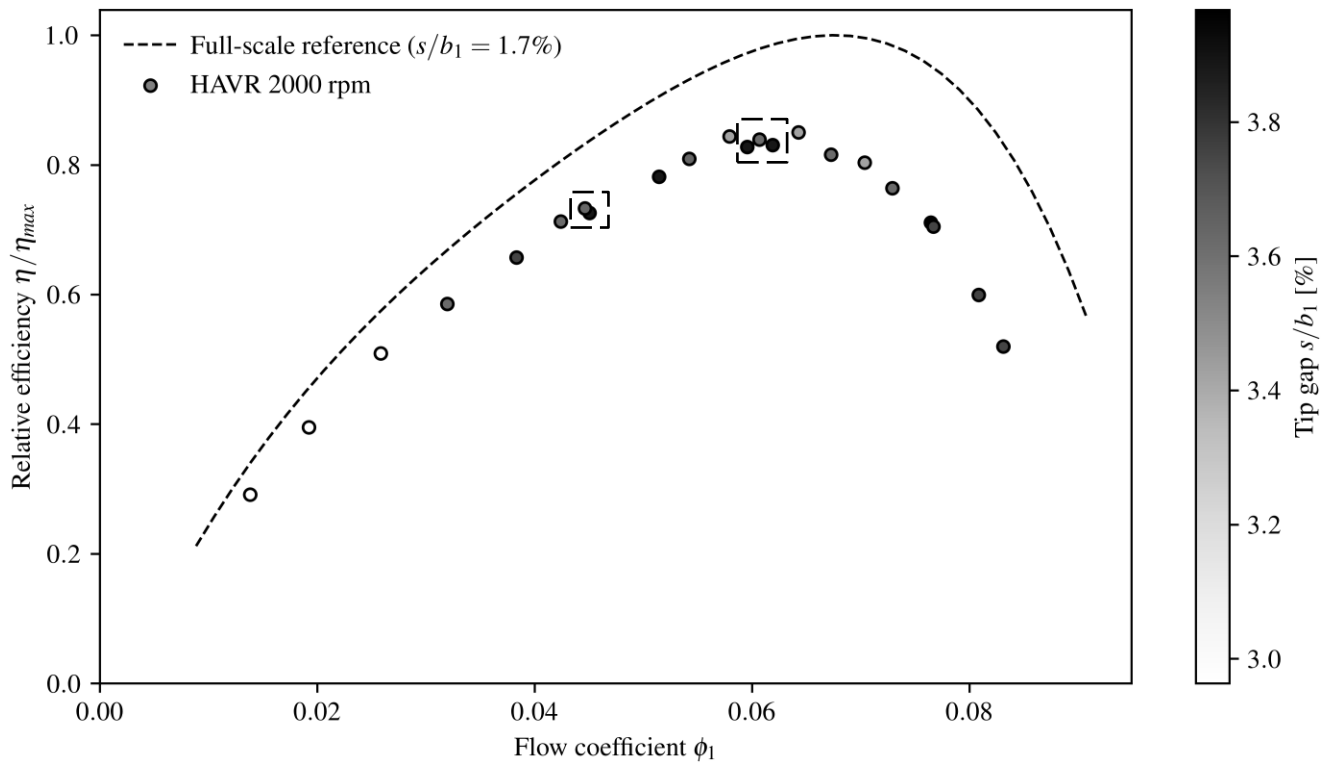


Figure 15. Efficiency Comparison – Single Phase Water. Average Relative Impeller Tip Gap Given in Greyscale for Each Test Point.

The actual tip gap during testing was estimated by FEM after the tests and the relative value (average for the three impellers) is plotted as a greyscale for each test point. The gap varies from about 3 to 4 percent of the inlet blade height, depending on water temperature and the pressure in the closed volume between the pump casing and diffuser cylinders. The full-scale reference had an average relative tip gap of 1.7 percent. A dependency on the tip gap clearance can be identified from the series of points in the figure, as points with smaller tip gap exhibit a higher efficiency than those with larger tip gap.

This information can be utilized to investigate the impact of a variation in tip gap at a certain flow coefficient. The test points within each of the dashed squares in Figure 15 were recorded during the same test session, i.e. with the same Re_T and mechanical losses, but with a different pressure in the closed volume between the pump casing and diffuser cylinders. The data points have been compared to establish a relation for head and efficiency as a function of tip gap size. Assuming a linear relation, as supported by previous findings for open, axial impellers, e.g. Gülich (2020) & Sun, et al. (2022), the performance with geometric similarity, $s/b_1 = 1.7$ percent, can be estimated. This is shown for efficiency in Figure 16. Here, the HAVR results in Figure 15 are represented by a best-fit polynomial.

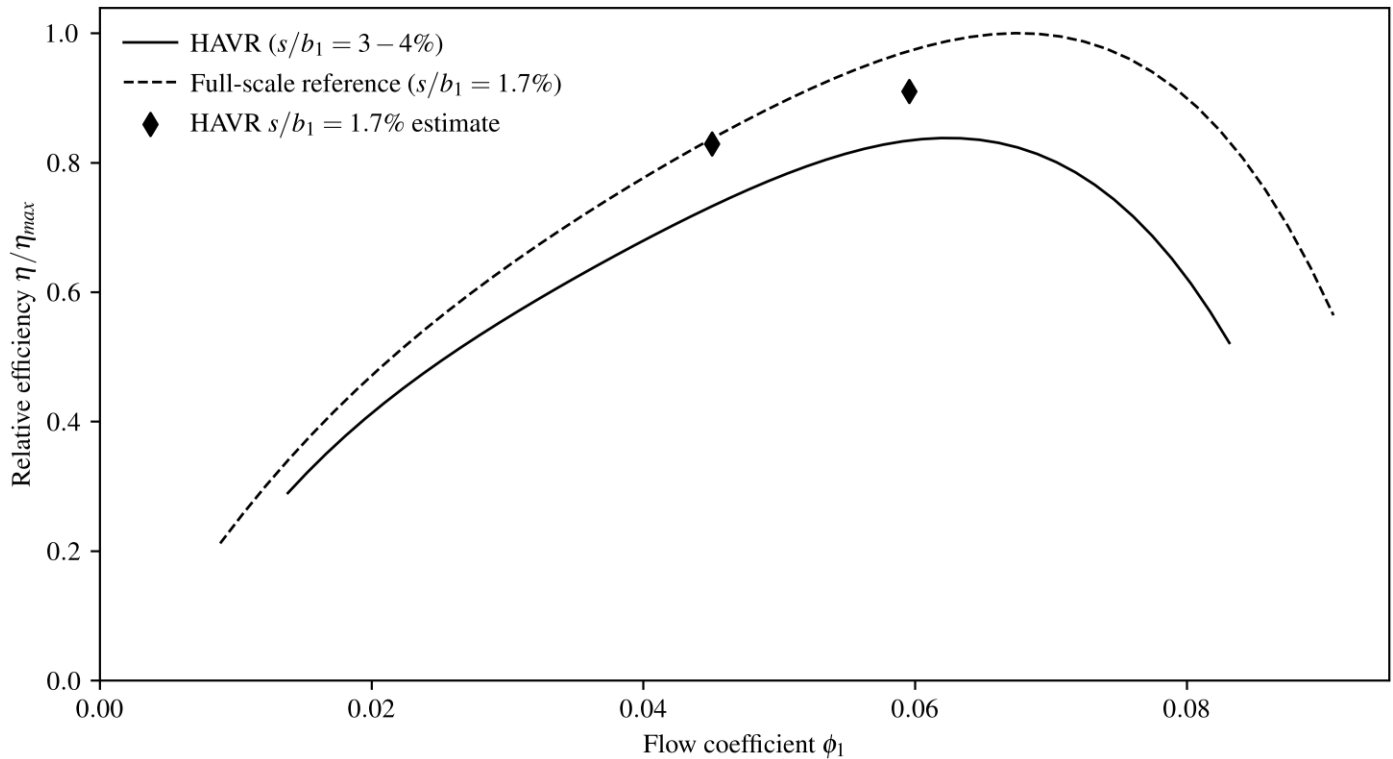


Figure 16. Single Phase Efficiency Comparison Including Estimated Efficiency with a Modified Impeller Tip Gap for Geometric Similarity with Full-Scale Setup

The estimate with geometric similarity brings the efficiency closer to the full-scale reference and one tendency is evident; From the two points it is seen that the relative impact of the tip gap size on the efficiency deficit is lower at the higher flow coefficient, where Reynolds number-dependent losses become increasingly important. The data can be related to results by d'Agostino, et al. (2017), who conducted tests with an unshrouded turbopump with a relative tip gap s/b_a equal to 0.9 and 11.2 percent, where b_a was the average blade height. The Reynolds number was kept at 5×10^6 . In terms of efficiency, the configuration with a large tip gap showed a decrease in efficiency relative to the one with a small tip gap for all tested flow coefficients. The difference increased with increasing flow coefficients. Considering the tested and estimated data in Figure 16, the same trend as found for the turbopump could be expected also for the helico-axial compression cell; Near the best efficiency point (BEP), and at higher flow coefficients, the increased tip gap of HAVR constitutes about half of the efficiency deficit relative to full-scale. At lower flow coefficients, the deficit decreases and can mainly be attributed to the variation in tip gap size. However, more data points where the relative tip gap is varied significantly at constant Re_T are needed to confirm this trend for the helico-axial impeller.

Figure 17 exhibits HAVR performance in terms of a best-fit polynomial for the 2000 rpm head-flow coefficient data points. The best efficiency points, evaluated from the curves in Figure 16, are indicated for HAVR and the full-scale reference. Estimated HAVR head coefficients with $s/b_1 = 1.7$ percent brings the head closer to the full-scale reference. It is seen that the head estimate at the lower flow coefficient is closer to the full-scale reference than the estimate at the higher flow coefficient. This indicates that the impact of tip gap size increases with lower flow rates where the losses related to tip leakage flow become dominant. At the higher flow rates, where the differential pressure across the impeller blades decreases, there is little to no leakage flow across the tip and the impact of tip gap size decreases. This finding is in line with results for the previously referenced turbopump (d'Agostino, et al. 2017) and a three-bladed axial inducer (Torre, et al. 2011).

The two estimated points can contribute to establish a model for the head coefficient as a function of relative tip gap size and flow coefficient. The model also assumes no head deficit due to tip gap size at maximum flow ($\psi = 0$) and no deficit due to Reynolds number effects at the minimum flow limit. It is indicated by a dash-dot curve for $s/b_1 = 1.7\%$ in Figure 17. More tests of other helico-axial impellers with varying specific speed could enable a general formulation of the model at a later stage.

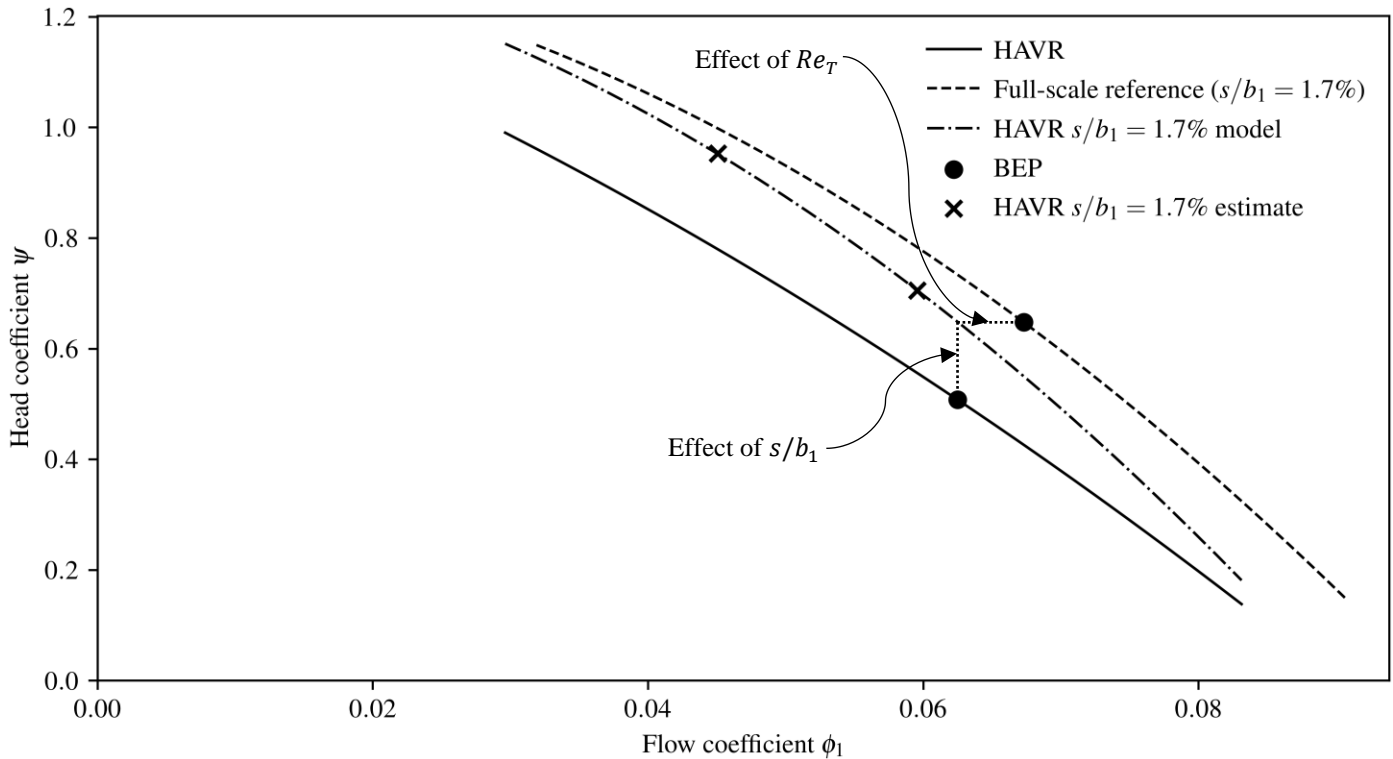


Figure 17. Single Phase Head Coefficient Comparison Including Model for Adjusted Tip Gap Size, Matching the Full-Scale Geometry

Test results for the unshrouded turbopump by d'Agostino, et al. (2017) show no significant shift in flow coefficient for BEP when varying the tip gap size. Applying the same result to the helico-axial pump fits well with the tested BEP as seen in Figure 17; The full-scale head coefficient in BEP matches the modeled head coefficient, suggesting that the flow coefficient for BEP is mainly shifted due to variations in Reynolds numbers.

With a model established for the HAVR head-flow curve at 1.7 percent tip gap, the remaining deficit compared to full-scale results can be further investigated. Morrison and Patil (2017) described a modeling approach for how to account for Reynolds-number effects on pump performance. The head coefficient can be described as a function of flow coefficient multiplied by the impeller tip-speed Reynolds number raised to a certain negative power, denoted the Morrison number, Mo . Mo depends on the pump geometry and whether the flow is laminar or turbulent. It can be found by comparing head-flow data recorded at different Reynolds numbers.

Figure 18 exhibits that the modeled head coefficient overlaps with the full-scale reference when plotted as a function of $\phi_1 Re_T^{-0.03}$, i.e. when

$$Mo = 0.03. \quad (6)$$

This number is lower than what was found for other pumps with similar specific speeds in Patil and Morrison (2019). The concept of an unshrouded impeller is not conventional in this range of specific speeds and the relatively strong influence of the tip leakage flow on the internal flow field can explain the deviation from referenced geometries.

The above relationship can be used to predict the pump's head coefficient in turbulent flow at different spatial scales, speeds and fluid properties, including for viscous fluids. The curves overlap well for all tested values of $\phi_1 Re_T^{-0.03}$, which adds confidence to the tip gap model shown in Figure 17. A set of HAVR test results is also shown in Figure 18. The deviation from the full-scale reference can now be attributed to the increased tip gap size. The impact of average tip gap size on the HAVR head coefficient results can be identified by comparing the greyscale information for each test point.

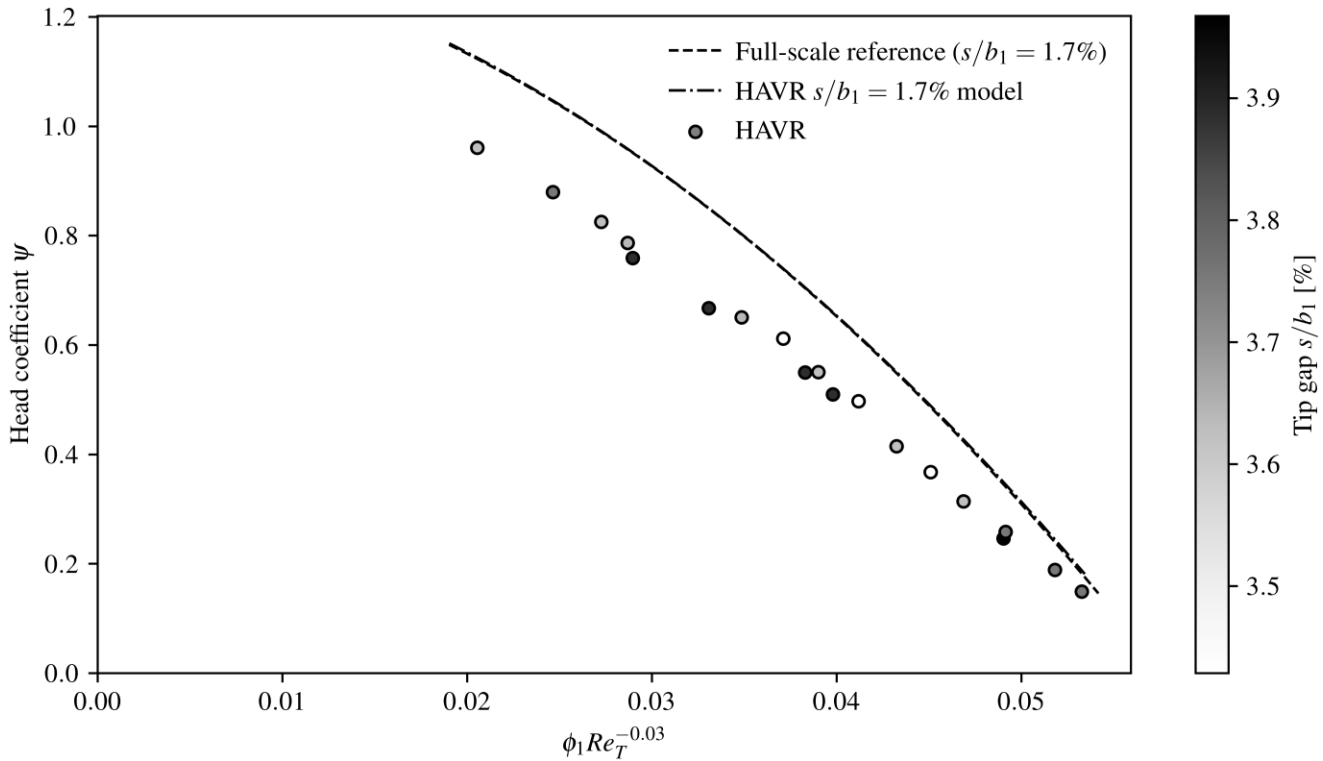


Figure 18. Single Phase Head Coefficient as a Function of Flow Coefficient and $Re_T^{-0.03}$ to Account for Reynolds Number Variations. Effect of Tip Gap Size on Head Coefficient Illustrated by HAVR Test Points with Greyscale.

With the knowledge of the location of the best efficiency points, the head coefficient can also be plotted in terms of relative flow rate, as seen in Figure 19. HAVR results are represented by best-fit polynomials. Of importance is that the shift from a negative slope of the curve at low relative flow occurs at the same relative flow rate for both HAVR and the full-scale reference. At maximum flow, the curves converge towards approximately the same relative flow rate. ϕ_{1BEP} is 0.0625 for HAVR and 0.0673 for the full-scale reference.

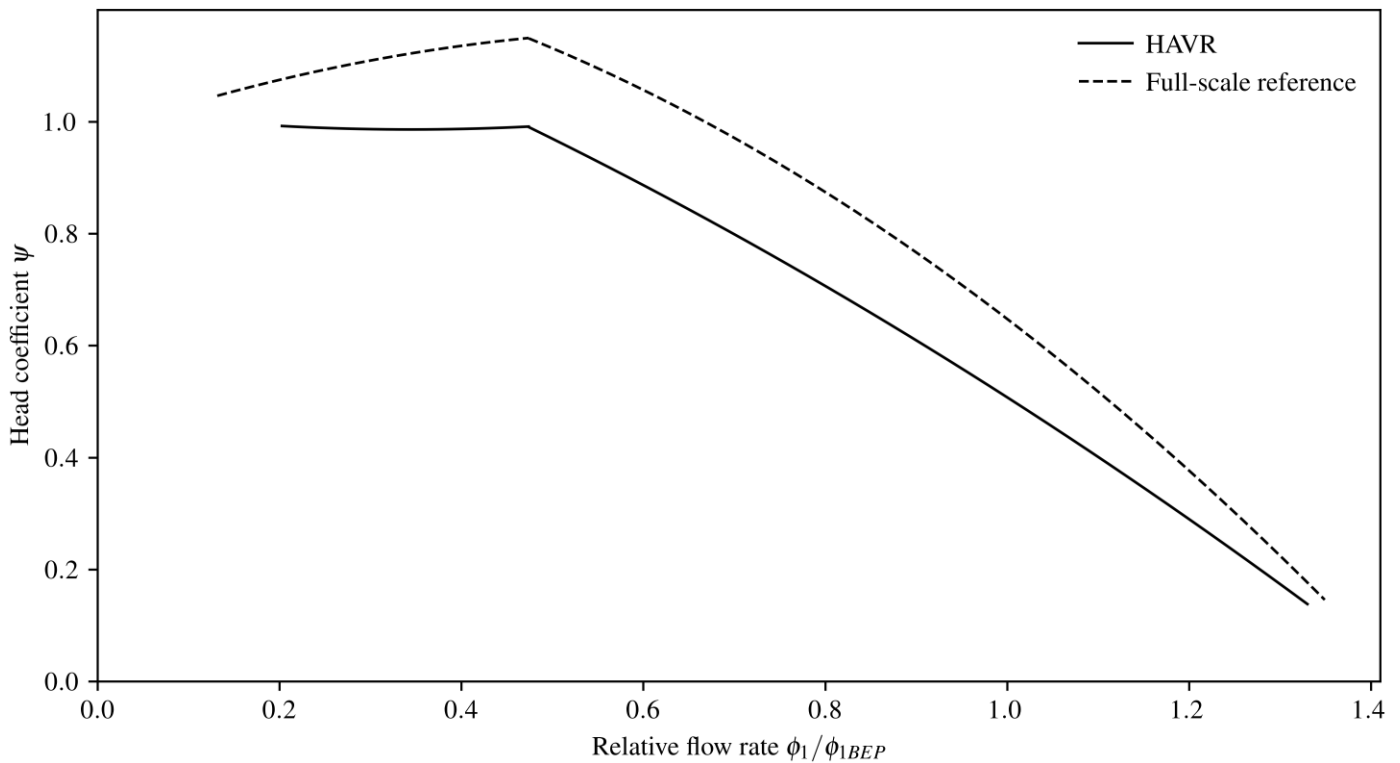


Figure 19. Single Phase Head Coefficient Comparison – Relative Flow Rate

Multiphase Operation

A controlled amount of nitrogen gas was injected through the ports in the pump unit inlet flange to operate HAVR in multiphase conditions. The gas enters an outer annulus in the pump unit inlet section and is mixed with liquid which is flowing in parallel in an inner annulus. The two annuli have a small inclination and are joined directly upstream the inlet guide vanes. Figure 20 depicts HAVR under multiphase operation with the water-filled visualization box installed on the pump casing. The picture was taken by a conventional camera and gives an impression of the observations that can be made, even by the naked eye in real time. Note that the relatively long exposure time of the camera results in traces of the bubble movement. This can give an impression of a higher gas volume fraction (GVF) in the flow than what is the reality, but it can also serve to understand the flow pattern. GVF is defined as

$$GVF = \frac{Q_g}{Q_l + Q_g} = \frac{Q_g}{Q}. \quad (7)$$

The inlet GVF in Figure 20 is about 2 percent. The pump speed is 1500 rpm and the relative flow rate is around 0.6. Note that, especially during part-load operation, the local void fraction in the compression cells can be higher than the inlet GVF.

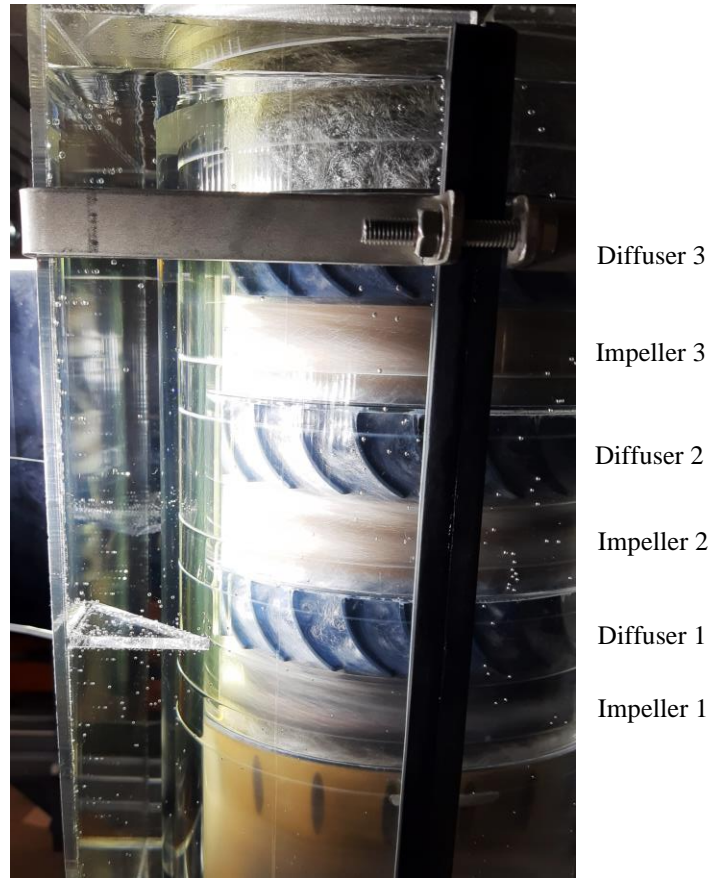


Figure 20. View of HAVR Under Multiphase Operation with Water-Filled Visualization Box Installed on Pump Casing. Inlet GVF About 2 Percent. Pump Speed 1500 rpm, Part-Load Operation.

The purpose of the test conditions seen in Figure 20 was to study the characteristics of the flow in the compression cells at very low GVF. Bubbly (or dispersed bubbly) flow was observed throughout the pump and the bubble size inside the compression cells was in the order of 0.5 mm. Several relative flow rates were tested and a high-speed camera was used to capture the dynamics of the flow in the second-stage impeller and diffuser. These recordings and the related analysis are yet to be published, but some flow features can already be discerned from Figure 20.

Figure 21 displays a closer view of the first diffuser and second impeller, taken from Figure 20. A significant impeller tip leakage flow was observed, resulting in backflow along the shroud and into the upstream diffuser channels. A counterclockwise recirculation zone on the pressure side of the diffuser vane was initiated by the backflow. A dynamic and relatively chaotic flow pattern was observed at the suction side of the diffuser vanes. Separation from the wall and a related clockwise recirculation zone was seen. Some accumulation of gas bubbles occurred in the vortices, including in what appears to be the impeller leading edge tip vortex. High-speed camera recordings can reveal more details and how these flow features depend on relative flow rate and the periodic blade passing. Note that a few larger bubbles can be seen in the figure. These are static air bubbles located in the walls within the visualization box, not internally in the compression cells.

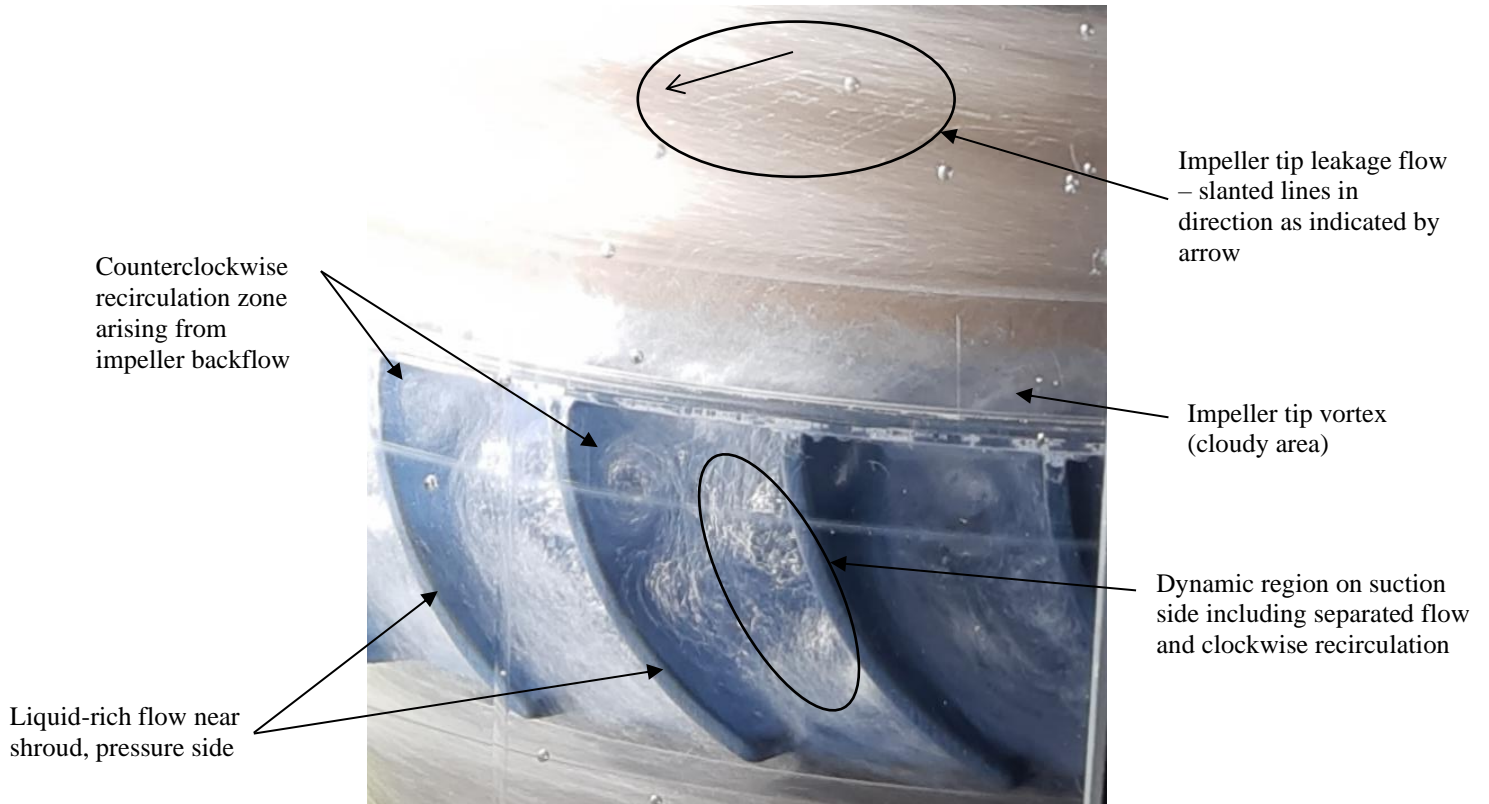


Figure 21. Portion of Figure 20, Illustrating Flow Features in Diffuser 1 and Impeller 2 at Part-Load Conditions.

The differential pressure generated by the pump at different GVF and pump total inlet flow rates is shown in Figure 22. For clarity, only data points from operation at 2000 rpm are shown. The pump inlet pressure and temperature were 1.7 bara and 24° C, respectively.

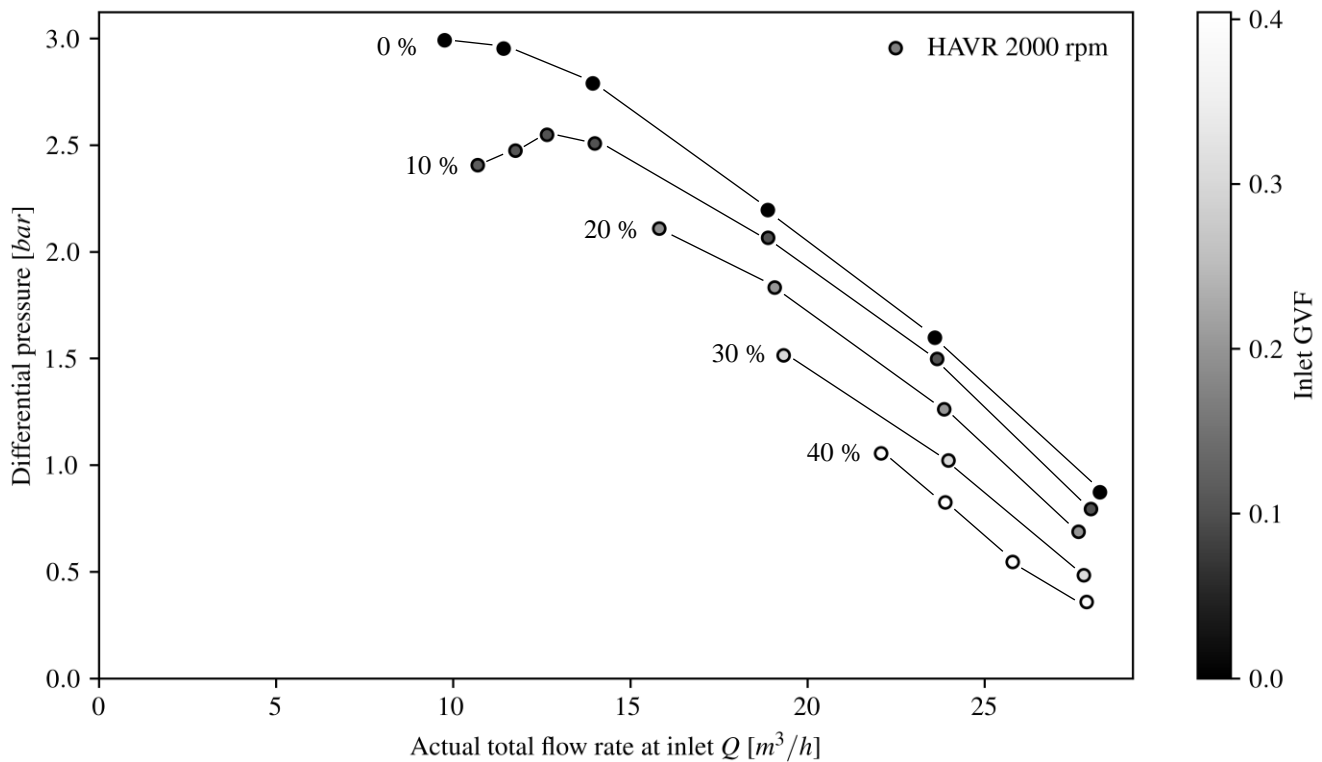


Figure 22. HAVR Differential Pressure – Multiphase Water & Nitrogen. Inlet GVF in Greyscale. Each Test Curve Identified by Notes of Approximate Inlet GVF. Inlet Pressure and Temperature: 1.7 bara, 24° C.

The multiphase efficiency is calculated by assuming ideal gas and isothermal compression:

$$\eta = \frac{Q_l dp + Q_g p_1 \ln(p_2/p_1)}{\Omega T} \quad (8)$$

The results are shown in Figure 23.

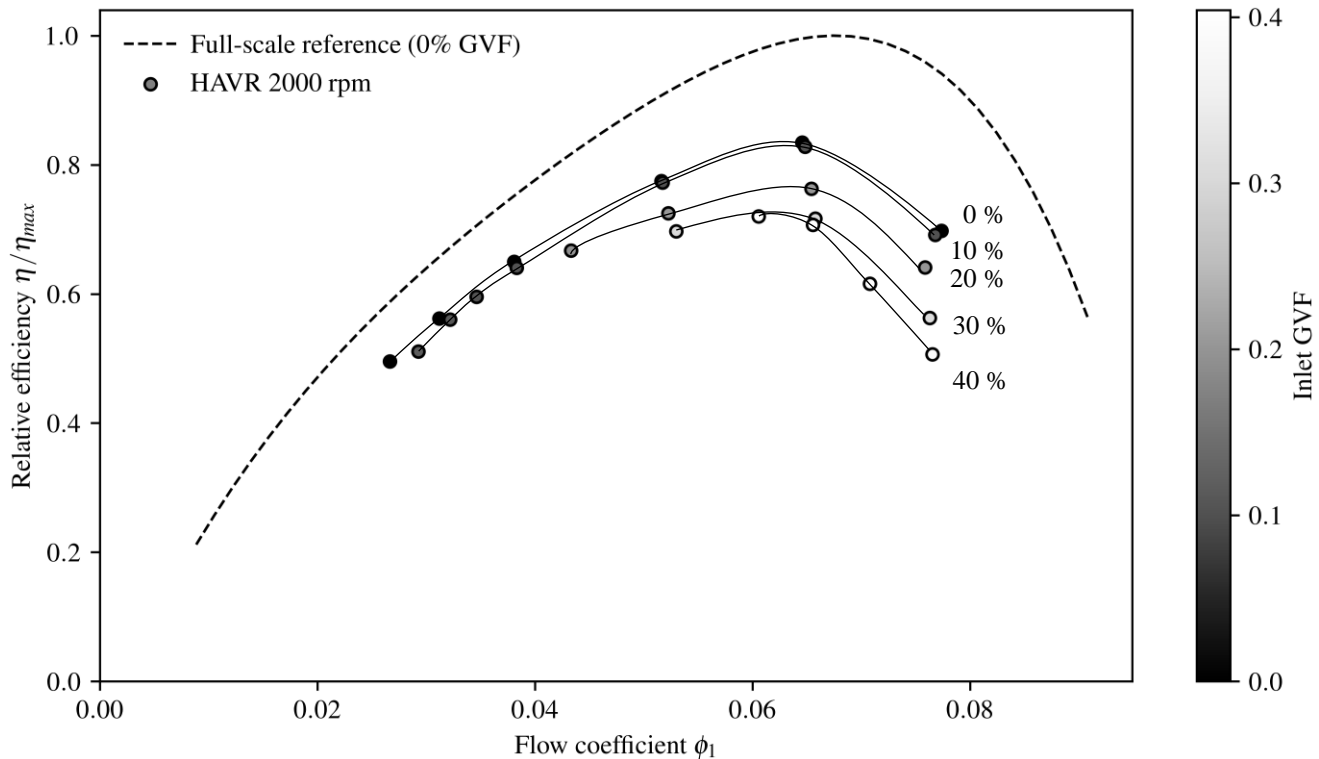


Figure 23. Isothermal Relative Efficiency for Single Phase and Multiphase Operation of HAVR at 2000 rpm. Flow Coefficient based on Total Flow Rate. Inlet Pressure and Temperature: 1.7 bara, 24° C. The Full-Scale Reference is for Single Phase Conditions.

Results for inlet conditions with up to approximately 40 percent GVF are shown. For reference, the gas mass fraction at 40 percent GVF is 0.0013. A reduction in differential pressure as the gas fraction increases is evident from Figure 22. This is first and foremost related to the reduced density of the fluid mixture at higher GVF. Secondly, a reduction in head (often denoted efficacy) is expected with increasing GVF, mainly due to slip between the phases (Falcimaigne and Decarre 2008). The reduction is most severe when the density ratio ρ_l/ρ_g is high. Figure 23 shows an almost insignificant reduction in efficiency at 10 percent GVF, compared to the single phase results. This indicates that the fluid is well mixed with little or no slip between the phases. However, moving from 10 to 20 percent GVF yields a more significant drop in efficiency, likely related to an observed change in flow regime. Note also that the efficiency at 30 and 40 percent, near BEP, is comparable, indicating a similar flow regime for the two conditions. The flow regimes at different GVF can be further studied with high-speed camera recordings to determine their relation to pump efficiency.

The efficacy of HAVR could be estimated with the assumption of equal performance of each stage, but full-scale results have shown that this is likely an invalid assumption due to the difference in inlet conditions at the first stage relative to the second and third stage. Interstage pressure measurements are thus needed to provide sufficient data to define the efficacy of a compression stage in HAVR. Implementation of interstage pressure ports is challenging in the acrylic glass pump casing due to the risk of cracks and thereby failure at elevated pressure. Another pump casing in aluminum is being engineered at the time of writing and can be used in future testing if stage hydraulic performance is the main object of interest, rather than flow visualization.

When comparing single phase and 10 percent GVF data points in Figure 22, a shift in flow rate for where the curve slope is no longer negative can be identified. At 10 percent GVF, a positive slope of the curve is now evident at flow rates below this point, whereas for single phase operation the curve was relatively flat. One contributing factor to this could be coalescence of gas in a region of low pressure and potentially stalled flow in the impeller. This implies increased slip between the phases and poorer head generation. The effect is amplified due to an increased GVF also in the downstream compression stages.

The actual volumetric flow rate will decrease through the pump due to compression of gas. The minimum flow rate, defined at pump inlet, will therefore increase with higher GVF to ensure that all compression cells operate within the specified limit, e.g. where the head-flow curve has a negative slope. When the slope of the curve becomes positive, the process flow system may become quasistatically

unstable (Brennen 2011). When compressible fluids are involved, this can easily lead to surge conditions where the pressure and flow rate varies significantly at relatively low frequencies. In a closed multiphase system this will normally result in slugging and a thus a high variation in differential pressure generated by the pump. From the multiphase results it is seen that stable operation with a positive slope of the head-flow curve was not possible at 20 percent GVF and higher. The flow rate required to maintain stable operation was increasing with higher GVF and above 40 percent GVF it was challenging to obtain additional performance data at BEP and lower flow rates. Figure 24 shows the limit where surge occurred, compared with the nominal minimum flow rate (i.e. the flow rate of the transition to a flat head-flow curve in Figure 19) due to compression at the relevant GVF and suction pressure.

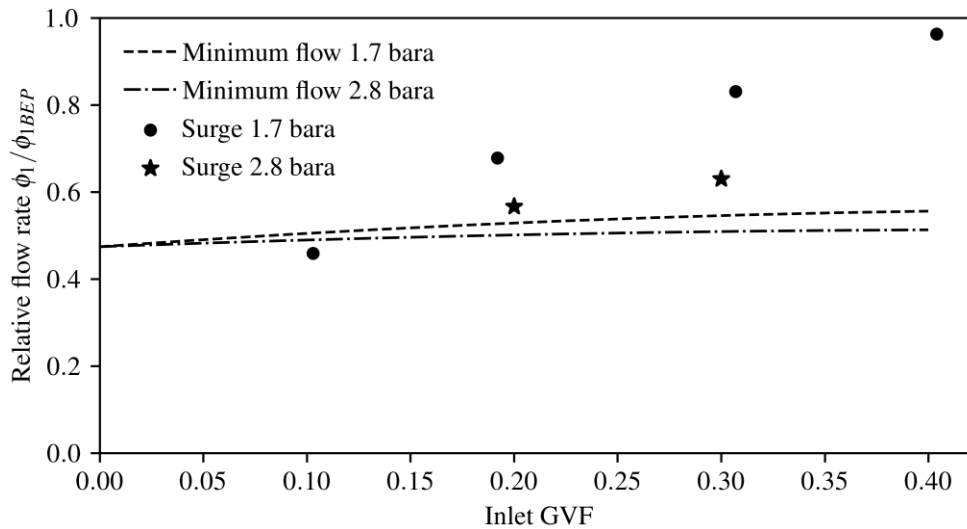


Figure 24. Relative Flow Rates where Surge Occurred for HAVR at Different Inlet Pressures, vs the Nominal Relative Minimum Flow Rate

There is a discrepancy between the test experience and the nominal value for the minimum flow rate. At low relative flow rate, the system is not able to operate at steady state conditions, even though the head-flow curve slope is presumably still negative. This indicates that the system is dynamically unstable, meaning there is a negative damping in the system. It could then easily become unstable due to perturbations in the flow. Dynamic instability analysis could give further insight to the system's behavior, as described by Brennen (2011) and Greitzer (1981). Such an analysis is not trivial for the current multiphase system, but several factors mentioned in the literature are relevant for the HAVR design. These include the mixing of the phases, impeller tip-speed, the strength of the tip clearance flow and the suction pressure (related to volumetric expansion of gas).

Figure 24 includes a second set of test points where the suction pressure and temperature was increased to 2.8 bara and 34° C, respectively. Although the nominal minimum flow rate is slightly lower at these conditions, a significant improvement in stable operating range is observed for the tested conditions at 20 and 30 percent GVF. Specifically, at 30 percent GVF, the relative flow rate where surge occurred was moved from 0.81 at 1.7 bara to 0.63 at 2.8 bara. Three main effects are associated with the change in suction conditions: A lower phase density ratio, normally improving efficacy. A larger tip gap size due to the increased pressure and temperature, leading to a higher redistribution rate and a more uniform pressure among the impeller channels. Finally, the higher absolute pressure results in less volumetric expansion of gas in low-pressure zones, that could obstruct the flow. This is naturally most relevant for the conditions in the first impeller, where the pressure is lowest. The importance of each of the three effects remains to be quantified, but it seems evident that a higher suction pressure contributes to avoid surge and widen the pump's operational envelope. This is in line with results found in the literature, e.g. by Gamboa and Prado (2010), where a mixed-flow compression cell was tested in a range of multiphase conditions with several combinations of fluids. Both an increased suction pressure and increased speed contributed to better gas-handling capabilities and a wider envelope for the mixed-flow cell. For HAVR, comparing results at 1500 and 2000 rpm yielded no significant difference in the relative flow rate where surge occurred.

The vertical annulus for the gas phase in the pump inlet section was initially filled with water, as the pump was always started in single phase conditions. The inlet section was semi-transparent, and when injecting small amounts of gas (GVF < 5 percent), a bubbly flow could be identified in the gas annulus. When injecting significant amounts of gas (GVF = 10 percent and above), an unsteady two-phase flow regime was observed. Hence, the gas flow rates were not high enough to flush the liquid phase out of the annulus. Assessing the operational conditions where surge occurred for HAVR, yields superficial gas velocities in the annulus in the range of 0.1 to 1 m/s. Following the results of Caetano, et al. (1992) for two-phase flow regimes in a vertical annulus, these numbers fall within the range where slug flow was observed when the superficial liquid velocity was low. Such a flow regime, with large bubbles, would lead to significant variations in the GVF entering the inlet guide vanes, both in time and circumferentially. If the flow is not sufficiently mixed through the inlet guide vanes, the impeller will also experience similar abrupt variations in inlet conditions. Such perturbations away from the steady operating conditions could be large enough to trigger surge in the system.

CONCLUSIONS

A multiphase pump visualization test rig has been designed and built for experiments with helico-axial unshrouded impellers. The rig was commissioned with a set of three compression cells with a low specific speed, 50 percent downscaled relative to a set previously tested. An acrylic glass pump casing enables full visual access so that the flow field can be studied by high-speed camera and measured by laser Doppler velocimetry.

Geometric similarity with the full-scale impeller and diffuser was not achieved with respect to the radial clearance in the impeller tip gap. Generally, a larger relative tip gap size resulted in a reduced performance compared to full-scale results due to increased losses related to the leakage flow through the gap. Different thermal expansion coefficients for the impellers and acrylic glass could cause a tip gap clearance that varied with process fluid temperature. However, the test rig design allowed changes the tip gap size during operation by controlling the external pressure acting on the acrylic glass in the diffuser stack. Sensitivity with regards to head and efficiency was investigated for two relative flow rates at zero percent GVF and the performance with geometric similarity could be estimated. This gives an impression of the impact of the tip gap versus losses related to lower Reynolds numbers over a range of flow coefficients. The data was used to find a Morrison number $Mo = 0.03$ for the present helico-axial pump, which can be used to predict pump performance also at other Reynolds numbers.

The tested head and efficiency, as a function of flow coefficient, resemble the full-scale reference data. The minimum flow rate, where the head-flow curve no longer exhibits a negative slope, occurred at the same relative flow rate as for the full-scale design. Multiphase test results are documented for conditions up to 40 percent GVF at pump inlet. Operation at low relative flow rates and high GVF led to system surge and slugging in the flow loop somewhat earlier than anticipated based on the minimum flow limit. Increasing the inlet pressure and temperature did however significantly improve the situation, allowing stable operation at lower relative flow rates. When injecting significant amounts of gas, large bubbles were observed upstream the inlet guide vanes. If they were not significantly broken down and mixed with the liquid phase through the inlet guide vanes, the first impeller would experience abrupt variations in inlet conditions, that could trigger system instability and thereby surge. The inlet design should be further studied and modified to avoid gas coalescence and thereby possibly widen the operational envelope at high GVF.

A preliminary investigation of the pump's internal flow field reveals several characteristic flow features. A bubbly flow is observed in the compression cells at 2 percent GVF. Bubble traces reveal the impeller tip leakage flow, which reaches upstream, into the adjacent diffuser outlet area, when operating at part-load conditions. Here the backflow contributes to a counterclockwise recirculation zone near the pressure side of the diffuser trailing edge. Flow separation from the suction side of the diffuser was also readily observed. Through this initial test campaign, HAVR has demonstrated its potential for flow visualization and hydraulic performance assessment. The results suggest that it can be used to reproduce the characteristics of the full-scale performance and flow field in multistage pumps with helico-axial impellers.

NOMENCLATURE

A	= Cross-sectional area	(L ²)
b	= Blade height	(L)
dp	= Differential static pressure	(M/LT ²)
g	= Gravitational constant	(L/T ²)
GVF	= Gas Volume Fraction	(-)
h	= Vertical distance between HAVR inlet and outlet	(L)
H	= Pump Head	(L)
N	= Specific speed	(-)
p	= Static pressure	(M/LT ²)
Q	= Actual volumetric flow rate	(L ³ /T)
Re	= Reynolds number	(-)
rpm	= Revolutions per minute	(T ⁻¹)
s	= Impeller tip gap (radial clearance)	(L)
T	= Torque	(ML ² /T ²)
β_b	= Blade angle (tangential reference)	(deg)
η	= Efficiency	(-)
μ	= Fluid dynamic viscosity	(M/LT)
ρ	= Fluid density	(M/L ³)
φ	= Flow coefficient	(-)
ψ	= Head coefficient	(-)
Ω	= Radian frequency of shaft rotation	(rad/T)

Subscripts

1	= Inlet (impeller or pump)
2	= Outlet
a	= Average
b	= Blade
D	= Design
g	= Gas
l	= Liquid
T	= Impeller tip

APPENDIX

Table 3 provides an overview of calibration data for different measurements.

Table 3. List of Instruments with Calibration Range and Maximum Error within Range After Calibration.

Measurement	Instrument type	Calibration range	Maximum error
Suction pressure p_1	Membrane	1.6 – 5.3 bara	0.4 %
Discharge pressure p_2	Membrane	1.5 – 5.3 bara	0.5 %
Liquid flow rate	Coriolis	5 – 40 m ³ /h	0.7 % at 5 m ³ /h 0.1 % at 15 - 40 m ³ /h
Gas flow rate – small range	Thermal, by-pass mass flow meter and controller	0.04 – 2 m ³ /h at standard conditions	0.5 % + 0.1 % full scale
Gas flow rate – medium range	Thermal, by-pass mass flow meter and controller	0.7 – 35 m ³ /h at standard conditions	0.5 % + 0.1 % full scale
Gas flow rate – large range	Inline thermal mass flow sensor and pilot-operated control valve	7 – 350 m ³ /h at standard conditions	1.0 % + 0.5 % full scale
Torque	Acoustic resonance	0 – 25 Nm	1.2 %
Speed	Optical switch (in torque meter)	Calibration based on laser Doppler velocimetry data at 1000 and 1500 rpm	0.0 %

REFERENCES

- Arnaudeau, M., 1993. Pumping or multiphase compression device and its use. *US Patent No. 5,375,976*.
- Barrios, L., 2007. Visualization and Modeling of Multiphase Performance Inside an Electrical Submersible Pump. Ph.D. Dissertation, The University of Tulsa, Petroleum Engineering Department.
- Bibet, P.-J., Lumpkin, V., Klepsvik, K., and Grimstad, H., 2013. Design And Verification Testing Of New Balance Piston For High Boost Multiphase Pumps. *Proceedings of the 29th International Pump Users Symposium*. Turbomachinery Laboratories, Texas A&M Engineering Experiment Station. Retrieved from <https://hdl.handle.net/1969.1/162569>
- Brennen, C. E., 2011. *Hydrodynamics of Pumps* (2nd ed.). Cambridge University Press.
- Caetano, E. F., Shoham, O., and Brill, J. P., 1992. Upward Vertical Two-Phase Flow Through an Annulus—Part I: Single-Phase Friction Factor, Taylor Bubble Rise Velocity, and Flow Pattern Prediction. *Journal of Energy Resources Technology*, 114(1), 1-13. doi:10.1115/1.2905917
- Cooper, P., Schiavello, B., de Marolles, C., de Salis, J., Prang, A. J., and Broussard, D. H., 1996. Multiphase Gas-Liquid Pumping. Texas A&M University. Turbomachinery Laboratories. doi:10.21423/R11X18
- d'Agostino, L., Valentini, D., Pasini, A., Torre, L., Pace, G., and Cervone, A., 2017. On the Preliminary Design and Performance Prediction of Centrifugal Turbopumps-Part 2. In *Cavitation Instabilities and Rotordynamic Effects in Turbopumps and Hydroturbines* (p. 175). Springer Cham. doi:10.1007/978-3-319-49719-8
- Dupoiron, M., 2018. The effect of gas on multi-stage mixed-flow centrifugal pumps. Doctoral Dissertation, University of Cambridge. doi:10.17863/CAM.20393
- El Hajem, M., Morel, R., Champagne, J., Vilagines, R., and Pagnier, P., 2001. The study of the flow in an helico-axial pump using laser Doppler velocimetry. *Houille Blanche*(3), 34-39.
- Falcimaigne, J. and Decarre, S., 2008. *Multiphase Production: Pipeline Transport, Pumping and Metering*. Paris: Editions Technip.
- Gamboa, J. and Prado, M. G., 2010. Visualization Study of Performance Breakdown in Two-Phase Performance of an Electrical Submersible Pump. Turbomachinery Laboratory, Texas A&M University. doi:10.21423/R1705B
- Greitzer, E. M., 1981. The Stability of Pumping Systems. *Journal of Fluids Engineering*, 103, 193-242.
- Gudigopuram, S. R., 2016. Experimental and CFD Simulation of a Helico-Axial Pump. Dissertation, Texas A&M University.

- Gülich, J. F., 2020. *Centrifugal Pumps* (4th ed.). Springer.
- Mansour, M., Parikh, T., Engel, S., Wunderlich, B., and Thévenin, D., 2019. Investigation on the Influence of an Inducer on the Transport of Single and Two-Phase Air-Water Flows by Centrifugal Pumps. *48th Turbomachinery and Pump Symposia*. Houston: Turbomachinery Laboratory, Texas A&M Engineering Experiment Station.
- Miyabe, M., Maeda, H., Umeki, I., and Jittani, Y., 2005. Unstable Head-Flow Characteristic Generation Mechanism of a Low Specific Speed Mixed Flow Pump. *Journal of Thermal Science*, 15(2).
- Morrison, G. L. and Patil, A., 2017. Pump Affinity Laws Modified to Include Viscosity and Gas Effects. *46th Turbomachinery & 33rd Pump Symposia*. Houston: Turbomachinery Laboratory, Texas A&M Engineering Experiment Station. Retrieved from <https://hdl.handle.net/1969.1/166770>
- Patil, A. and Morrison, G. L., 2019. Affinity Law Modified to Predict the Pump Head Performance for Different Viscosities Using the Morrison Number. *Journal of Fluids Engineering*, 141(2).
- Rapposelli, E., Cervone, A., and d'Agostino, L., 2002. A New Cavitating Pump Rotordynamic Test Facility. *38th AIAA/ASME/SAE/ASEE Joint Propulsion Conference & Exhibit*. Indianapolis: American Institute of Aeronautics and Astronautics, Inc.
- Serena, A. and Bakken, L. E., 2015. Design of a Multiphase Pump Test Laboratory Allowing to Perform Flow Visualization and Instability Analysis. *Proceedings of the ASME 2015 Power Conference* (pp. 1-11). San Diego, CA: ASME. doi:10.1115/POWER2015-49769
- Stenhaus, M., Dong, H., and Hjelmeland, M., 2019. Why Not Boosting? Uncover the True Value of Your Subsea Asset. *OTC Offshore Technology Conference*. Houston, TX. doi:10.4043/29407-MS
- Sun, W., Yu, Z., Zhang, K., and Lui, Z., 2022. Analysis of Tip Clearance Effect on the Transportation Characteristics of a Multiphase Rotodynamic Pump Based on the Non-Uniform Bubble Model. *Fluids*, 7(58). doi:10.3390/fluids7020058
- Torre, L., Pasini, A., Cervone, A., Pace, G., Miloro, P., and d'Agostino, L., 2011. Effect of Tip Clearance on the Performance of a Three-Bladed Axial Inducer. *Journal of Propulsion and Power*, 27(4), 890-898. doi:10.2514/1.B34067
- Vilagines, R., Pagnier, P., Akhras, A., El Hajem, M., Champagne, J., and Morel, R., 2003. A Study of the Flow in a Helical-Axial Pump Rotor. *The 12th International Conference on Fluid Flow Technologies*. Budapest, Hungary: CMFF'03.
- Xu, Y., Cao, S., Sano, T., Wakai, T., and Reclari, M., 2019. Experimental Investigation on Transient Pressure Characteristics in a Helico-Axial Multiphase Pump. *Energies*, 12(461), 1-20. doi:10.3390/en12030461
- Zhang, J., Cai, S., Zhu, H., and Zhang, Y., 2015. Experimental investigation of the flow at the entrance of a rotodynamic multiphase pump by visualization. *Journal of Petroleum Science and Engineering*, 126, 254-261. doi:10.1016/j.petrol.2014.12.017
- Zhang, J., Li, Y., Cai, S., Zhu, H., and Zhang, Y., 2016. Investigation of gas-liquid two-phase flow in a three-stage rotodynamic multiphase pump via numerical simulation and visualization experiment. *Advances in Mechanical Engineering*, 8(4), 1-13. doi:10.1177/1687814016642669

ACKNOWLEDGEMENTS

The present study was funded by OneSubsea, IFPEN and The Research Council of Norway.